

# Optical Interaction of Light with Semiconductor Quantum Confined States at the Nanoscale

T. Saiki

## 1.1 Introduction

Optical probing and manipulation of electron quantum states in semiconductors at the nanoscale are key to developing future nanophotonic devices which are capable of ultrafast and low-power operation [1]. To optimize device performance and to go far beyond conventional devices based on the far-field optics, the degree to which the electron and light are confined must be properly designed and engineered. This is because while stronger confinement of the electron lets us use its quantum nature, its interaction with light becomes weaker with reduction of the confinement volume. To maximize their interaction, we need the overlap in scale between confinement volume of electron and that of light. More generally, the spatial profile of the light field should be designed to match that of electron wavefunction in terms of phase as well as amplitude.

Semiconductor quantum dots (QDs) provide ideal electron systems because electrons are three-dimensionally confined. This results in a discrete density of states in which the level of energy spacing exceeds the thermal energy. Due to the nature of QDs, they exhibit ultranarrow optical transition spectrum and long duration of coherence [2, 3]. Moreover they can be engineered to have desired properties by controlling the size, shape and strains, as well as by selecting appropriate material. Regarding the size of QDs, with the maturation of crystal growth along with the nanofabrication of semiconductors, we have obtained QDs in a wide range of sizes from a few nm to larger than 100 nm. For example, interface fluctuation QDs—where excitons by imperfect GaAs quantum are well confined—are extensively studied [4]. By adopting a growth-interruption technique, monolayer-high islands larger than 100 nm develop at the well–barrier interface. Large QDs are advantageous for maximizing the magnitude of the light–electron (exciton) interaction due to the enhancement of oscillator strength, which is proportional to the size of QDs [5].

The progress in light confinement, on the other hand, has also been remarkable [6, 7]. Basically, efforts to focus light more tightly than half the wavelength (diffraction limit) have been motivated by the ultimate spatial resolution of optical microscopy. For example, a near-field scanning optical microscope (NSOM) [6, 7] uses a sharpened optical fiber probe with a small metal hole at its apex to squeeze light in an area determined by the size of the hole. Recent advances in fabrication of NSOM probes enable us to generate a light spot smaller than 10 nm [8]. An optical antenna is also attracting attention due to its higher efficiency in the delivery of energy to a nanofocused spot [9]. Metal nanorods and more sophisticated metal structures provide an opportunity to engineer the light field at the nanoscale with a high degree of freedom.

Broad overlap in the scale between the confinement volume of electrons and light, as described above, leads to changes in their interaction from the far-field counterpart [10]. More specifically, in the case where the spatial resolution of NSOM falls below the size of QD, it becomes possible to directly map out the distribution of the wavefunction [11]. More interestingly, the optical selection rule can be broken; one can excite the dark states whose optical transition is forbidden by the far field and can open new radiative decay channels. The light–matter coupling at the nanoscale offers guiding principles for future nanophotonic devices.

Here, we describe development of a high-resolution NSOM with a carefully designed aperture probe and near-field imaging spectroscopy of quantum confined systems. Thanks to a spatial resolution as high as 1–30 nm, we visualize spatial profiles of local density of states and wavefunctions of electrons confined in QDs and clarify the fundamental aspects of localized and delocalized electrons in interface and alloy disorder systems.

## 1.2 Near-Field Scanning Optical Microscope

### 1.2.1 General Description

When a small object is illuminated, its fine structures with high spatial frequency generate a localized field that decays exponentially normal to the object [6, 7]. This evanescent field on the tiny substructure can be used as a local source of light, illuminating and scanning a sample surface so close that the light interacts with the sample without diffraction. A metal opening (aperture) is a popular method for generating a localized optical field suitable for NSOMs. As illustrated in Fig. 1.1, aperture NSOM uses a small opening at the apex of a tapered optical fiber coated with metal. Light sent down the fiber probe and through the aperture illuminates a small area on the sample surface. The fundamental spatial resolution is determined by the diameter of the aperture, which ranges from 10–100 nm.

The simplest setup for imaging spectroscopy based on aperture NSOM is a configuration with local illumination and local collection of light through an aperture, as illustrated in Fig. 1.1. The light emitted by the aperture interacts with the sample locally. Resultant signals from the interaction volume must be collected as efficiently

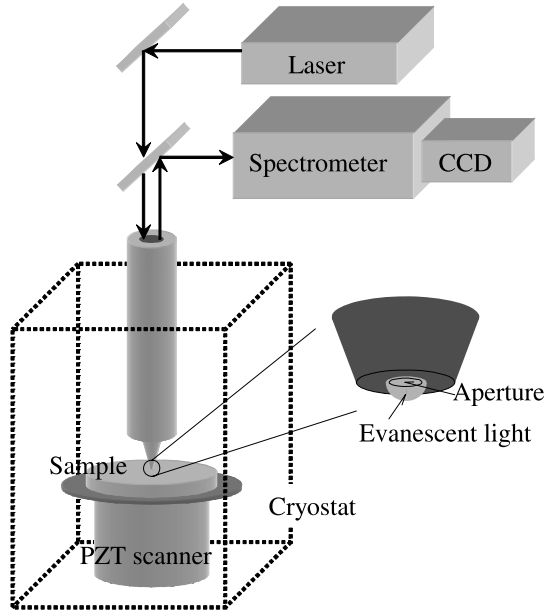


**Fig. 1.1.** A schematic illustration of standard NSOM setup with a local illumination and local collection configuration

as possible. In photoluminescence (PL) or Raman spectroscopy, the collected signal is dispersed by a spectrometer and is detected by a CCD recording device. The regulation system for tip-sample feedback are essential for NSOM performance, and most NSOMs employ a method similar to that used in an atomic force microscope (AFM), called shear force feedback, the regulation range of which is 0–10 nm [12]. For the measurement at low temperature to reduce phonon-induced broadening, the sample, probe tip, and scanner are placed into a cryostat [13].

### 1.2.2 Aperture-NSOM Probe

Great effort has been devoted to fabricating the aperture probe, which is the heart of NSOM. Since the quality of the probe determines the spatial resolution and sensitivity of the measurements, tip fabrication remains of major interest in the development of NSOM. To enhance the performance of aperture-NSOM, we focus on two important features of the probe: the light propagation efficiency of the tapered waveguide and the quality of aperture, as illustrated in Fig. 1.2.

Improvement in the optical transmission efficiency (throughput) and collection efficiency of aperture probes is the most important issue to be addressed for the application of NSOM in the spectroscopic studies of nanostructures. The tapered region of the aperture probe operates as a metal-clad optical waveguide. The mode structure in a metallic waveguide is completely different from that in an unperturbed fiber and is characterized by the cutoff diameter and absorption coefficient of the

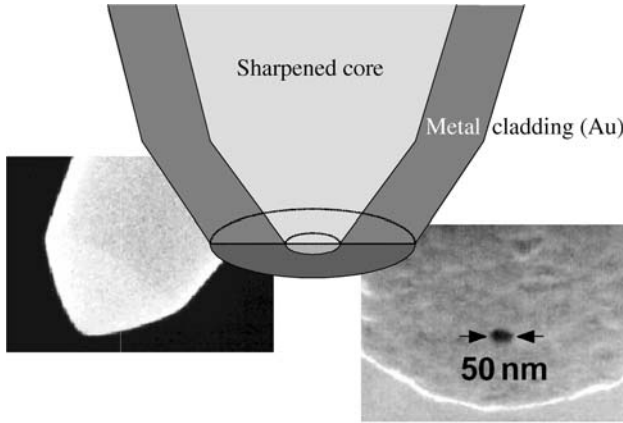


**Fig. 1.2.** A schematic illustration of aperture-NSOM probe. Scanning electron micrographs of a double-tapered probe (taken prior to metal coating) and a well-defined aperture are also shown

cladding metal. Theoretical and systematic experimental studies have confirmed that the transmission efficiency of the propagating mode decreases in the region where the core diameter is smaller than half the wavelength of the light in the core. The power that is actually delivered to the aperture depends on the distance between the aperture plane and the plane in which the probe diameter is equal to the cutoff diameter; this distance is determined by the taper angle. We therefore proposed a double-tapered structure with a large taper angle [14, 15]. This structure is easily realized using a multistep chemical etching technique, as will be described later. With this technique, the transmission efficiency is much improved by one to two orders of magnitude as compared to the single-tapered probe with a small taper angle.

We used a chemical etching process with buffered HF solution to fabricate the probe. The etching method is easily reproducible and can be used to make many probes at the same time. The details of probe fabrication with selective etching are described in [15]. The taper angle can be adjusted by changing the composition of a buffered HF solution. A two-step etching process is employed to make a double-tapered probe. Another important advantage of the chemical etching method is the excellent stability of the polarization state of the probe.

The next step is metal coating and aperture formation. In general, the evaporated metal film generally has a grainy texture, resulting in an irregularly shaped aperture with nonisotropic polarization behavior. The grains also increase the distance between the aperture and the sample, not only degrading resolution but also reducing the intensity of the local excitation. As a method for making a high-definition aperture probe, we use a simple method based on the mechanical impact of the metal (Au) coated tip on a suitable surface [16, 17]. The resulting probe has a flat end and a well-defined circular aperture. Furthermore, the impact method assures that the aperture plane is strictly parallel to the sample surface, which is important in minimizing the distance between the aperture and the sample surface. The size of the aperture

can be selected by carefully monitoring the intensity of light transmitting from the apex, since the throughput of the probe is strictly dependent on the aperture diameter.

### 1.3 Spatial Resolution of NSOM Studied by Single Molecule Imaging

Ultimate spatial resolution of NSOM is of great interest from the viewpoint of revealing the nature of light–matter interaction at the nanoscale. As a standard method for the evaluation of spatial resolution of NSOM, fluorescence imaging of a single molecule is most reliable because it behaves as an ideal point-like light source. Many groups have made efforts to improve the resolution in the single-molecule imaging using a variety of methods, such as apertureless NSOM [18] and a single molecule light source [19]. A spatial resolution as high as 32 nm has been reported in fluorescence imaging by using a microfabricated cantilevered probe [20]. By using an aperture probe, a spatial resolution as high as 25 nm has been reported recently in single molecule fluorescence imaging by scanning near-field optical/atomic force microscopy [21].

In this section, we describe single-molecule imaging with a high resolution of approximately 10 nm achieved by an aperture NSOM [22]. To discuss the depen-

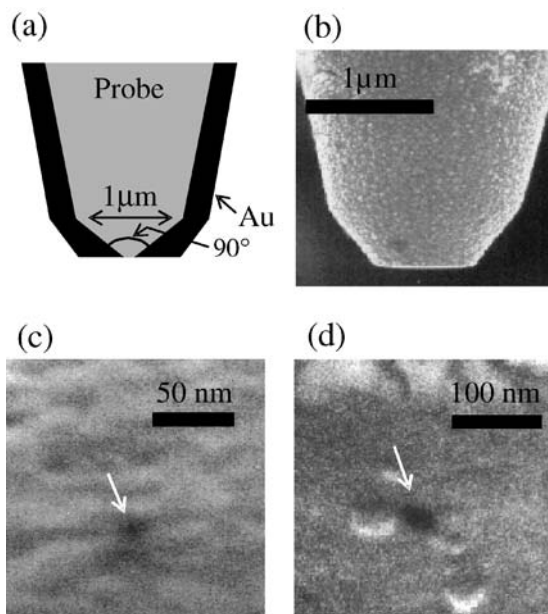


**Fig. 1.3.** **a** A cross-sectional illustration of the Au-coated probe. **b–d** Scanning electron micrographs of aperture probes: **b** a side view of a probe with the double-tapered structure; **c–d** apertures created by the impact method. Aperture diameters are 10 and 30 nm, respectively

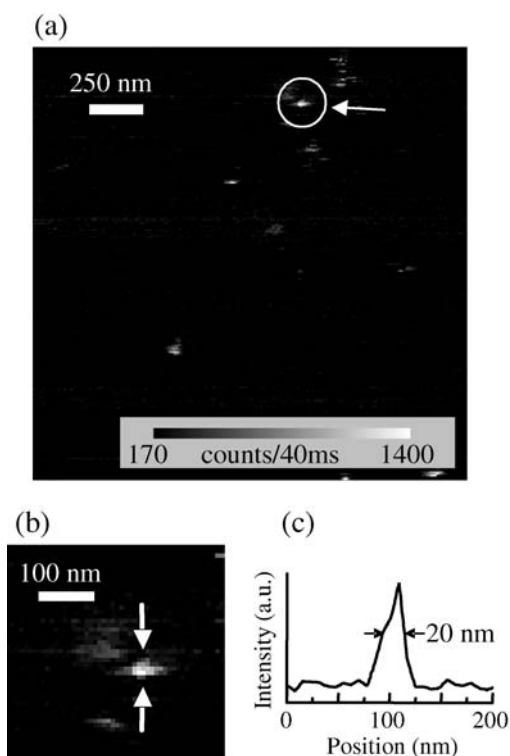


**Fig. 1.4.** **a** A fluorescence image of single Cy5.5 molecules at 633-nm excitation. **b** A magnified image of the bright spot circled in **a**. **c** A cross-sectional profile of the signal intensity evaluated along a line indicated by the pair of arrows in **b**. The spatial resolution determined from the FWHM of the profile is 20 nm

dence of the resolution on the wavelength of excitation light, measurements with two different excitation lasers for the same probes are carried out. These results are compared with a computational calculation employing the finite-difference time-domain (FDTD) method, which is appropriate for simulating electromagnetic field distributions applied to actual three-dimensional problems [23]. Thus we discuss the achievable spatial resolution of the aperture NSOM.

### 1.3.1 Single-Molecule Imaging with Aperture Probes

An NSOM fiber probe with the double-tapered structure and well-defined aperture created by the mechanical impact method, as described in Sect. 1.2, was employed. Samples examined were single dye molecules of Cy5.5 and Rhodamine dispersed on quartz substrates. Single-molecule dispersion on the substrate was confirmed by observing one-step photobleaching of almost all of the molecules. The fluorescence NSOM was operated in the illumination mode. As excitation light sources, a He-Ne laser ( $\lambda = 633$  nm) and a SHG YVO<sub>4</sub> laser ( $\lambda = 532$  nm) were employed. The

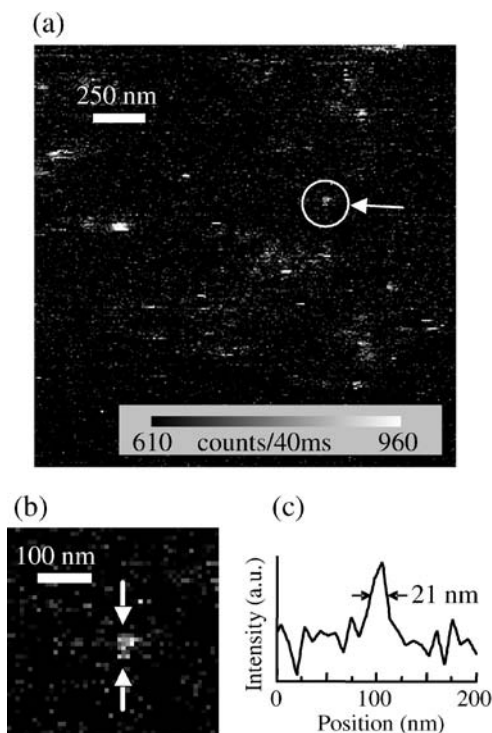


**Fig. 1.5.** **a** A fluorescence image of single Cy5.5 molecules at 532-nm excitation obtained using the same probe and the same sample as those in Fig. 1.4, but not measured in the same area as in Fig. 1.4(b). A magnified image of the bright spot circled in **a**. **c** A cross-sectional profile along a line indicated by the pair of arrows in **b**. The spatial resolution is estimated to be 21 nm

emission from a single dye molecule was collected by an objective lens and transported to an avalanche photodiode (APD) through a bandpass filter (center wavelength  $\lambda = 700$  nm, bandwidth  $\Delta\lambda = 40$  nm for the Cy5.5 dye,  $\lambda = 600$  nm,  $\Delta\lambda = 40$  nm for the Rhodamine dye). The sample-probe distance was controlled by a shear-force feedback mechanism.

Figure 1.3(a) shows a cross-sectional illustration of the Au-coated probe. Scanning electron micrographs of aperture probes are shown in Figs. 1.3(b)–(d): a side view of a probe with the double tapered structure and overhead views of apertures. From the scanning electron micrographs, which were taken after several scanning measurements, we found the probes have flat end-faces with small round apertures. The diameters of the apertures in Figs. 1.3(c) and 1.3(d) are estimated to be 10 nm and 30 nm, respectively.

Figure 1.4(a) shows a fluorescence image of single Cy5.5 dye molecules irradiated by the He–Ne laser light. Each bright spot is attributed to the fluorescence from a single molecule. The bright spot circled in the image is magnified in Fig. 1.4(b).

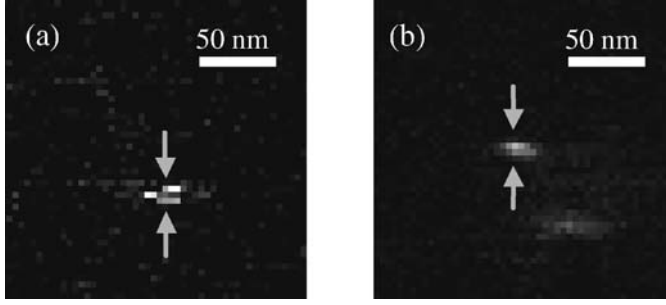


**Fig. 1.6.** The highest resolution images obtained with Rhodamine at 532-nm excitation (a) and Cy5.5 at 633-nm excitation (b). Estimated resolutions are 11 and 8 nm, respectively

Figure 1.4(c) shows a cross-sectional profile of the fluorescence signal intensity evaluated along a line indicated by a pair of arrows in Fig. 1.4(b). From the full width at half maximum (FWHM) of the profile, the spatial resolution is estimated to be 20 nm.

Figure 1.5(a) shows a fluorescence image obtained using the same probe and the same sample of single Cy5.5 dye molecules, but not measured in the same area as in Fig. 1.4(a), by the SHG YVO<sub>4</sub> laser excitation. The bright spot circled in Fig. 1.5(a) is magnified in Fig. 1.5(b), and Fig. 1.5(c) shows its cross-sectional profile. The spatial resolution estimated from the FWHM of the profiles is 21 nm.

The highest resolutions images obtained with Rhodamine at 532-nm excitation and Cy5.5 at 633-nm excitation are shown in Figs. 1.6(a) and 1.6(b), respectively. The resolution is estimated to be 11-nm at 532-nm excitation and 8-nm at 633-nm excitation.

### 1.3.2 Numerical Simulation of NSOM Resolution

To evaluate the achievable resolution of the aperture NSOM in visible range in the illumination mode of operation, a computer simulation by the FDTD method was employed for various aperture sizes and wavelengths. Electric fields ( $E$ ) were calculated for the probe tip with an aperture diameter  $D = 20$  nm at various wavelengths ( $\lambda = 405, 442, 488, 514.5, 532$  and  $633$  nm) of irradiation lights, and for the probe tips with various aperture sizes ranging from  $D = 0$  to  $50$  nm at the wavelength  $\lambda = 633$  nm.

Figure 1.7(a) illustrates a cross-sectional view of the FDTD geometry of the three-dimensional problem, which reproduces the tip of the double-tapered probe with an aperture employed in the experiments. A three-dimensional illustration of the probe is shown in Fig. 1.7(b). The origin of the Cartesian coordinate was located at the center of the aperture. We assumed the light source, which was placed at 10 nm below the upper end of the tapered probe with a cone angle  $\theta = 90^\circ$ , was a plane wave with a Gaussian distribution polarized along the  $x$  direction. The refractive index of the core of the fiber was 1.5 and the refractive indices of the real Au metal were extracted from [24]. The simulation box had a size of  $1.6 \times 1.6 \times 0.8 \mu\text{m}^3$  in



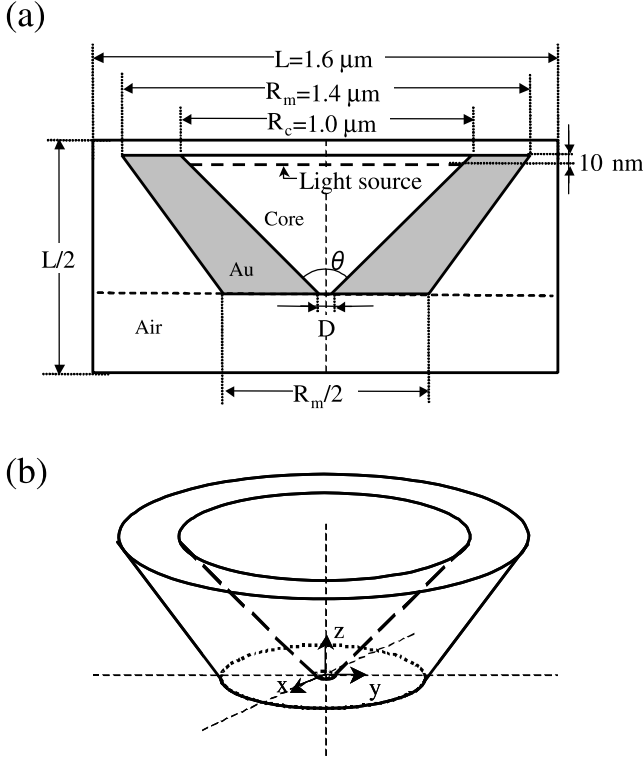


**Fig. 1.7. a** An illustration of the cross-sectional view of the FDTD geometry of three-dimensional problem, which reproduces the experimental situation. **b** A three-dimensional illustration of the tapered probe

the  $x$ ,  $y$  and  $z$  directions. The space increment of the  $z$  directions around the aperture was  $2 \text{ nm}$ , and the increments of the  $x$  and  $y$  directions were  $1 \text{ nm}$  for aperture diameters less than  $D = 10 \text{ nm}$ , and were  $2 \text{ nm}$  for the other aperture diameters.

Figures 1.8(a) and 1.6(b) show the intensity distribution of electronic field  $|E|^2$  along the  $x$ - and  $y$ -axes, respectively, on  $z = -4 \text{ nm}$  plane for the probe with the aperture of  $D = 20 \text{ nm}$  at  $\lambda = 633 \text{ nm}$  excitation. Here we define the spatial resolution of  $\Delta x$  and  $\Delta y$  as the FWHM of the intensity distribution, indicated by arrows in Figs. 1.8(a) and 1.8(b).

Spatial resolutions for the aperture of  $D = 20 \text{ nm}$  at various wavelengths are plotted in Fig. 1.9. The skin depth of Au calculated from its optical constants is indicated by a dashed line. It is found that the dependence of the resolution on the excitation wavelength has a similar tendency as the skin depth of Au. Figure 1.10 shows the resolutions for various aperture diameters  $D = 0, 10, 20, 30$  and  $50 \text{ nm}$  at  $\lambda = 633 \text{ nm}$ . The result indicates that the discrepancy between the predicted resolution and the physical aperture size is less than  $10 \text{ nm}$  for  $D > 10 \text{ nm}$ . The highest resolution is obtained at  $D = 10 \text{ nm}$  and is evaluated to be  $\Delta x = 16 \text{ nm}$  and  $\Delta y = 12 \text{ nm}$ .

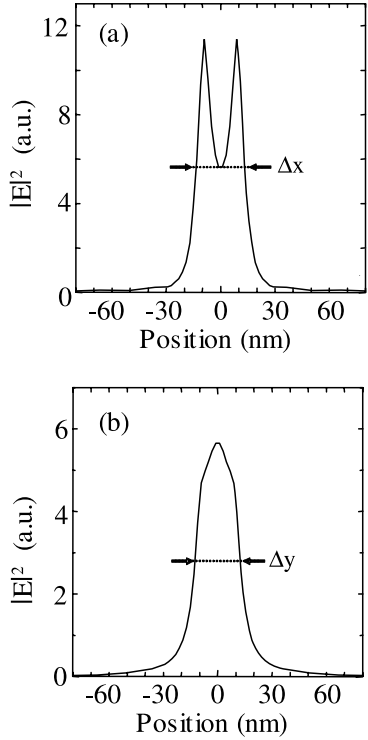


**Fig. 1.8.** The intensity distributions of electronic field along the  $x$ -axis **a** and the  $y$ -axis **b**, calculated on  $z = -4$ -nm plane for the probe with an aperture of  $D = 20$  nm at  $\lambda = 633$ -nm excitation. The spatial resolutions of  $\Delta x$  and  $\Delta y$  are defined as the FWHM of the intensity distributions indicated by the pairs of arrows

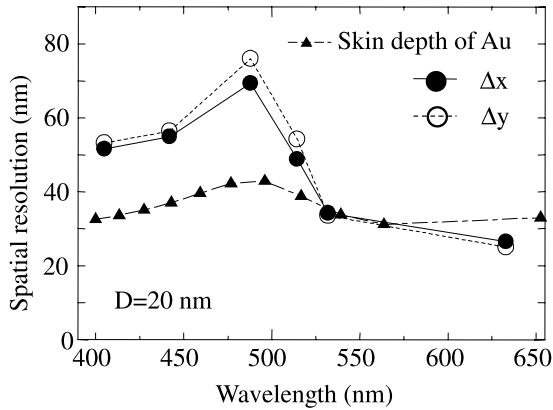


**Fig. 1.9.** Calculated spatial resolutions for the aperture with  $D = 20$  nm at various wavelengths

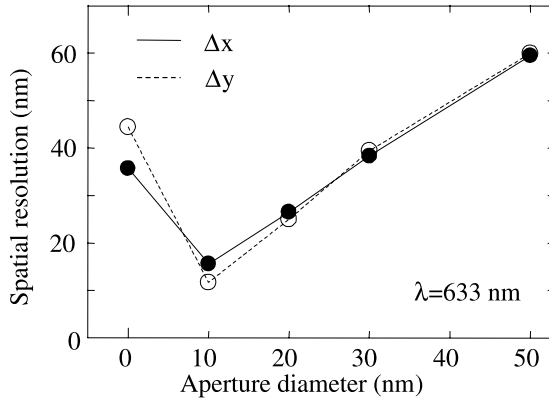


**Fig. 1.10.** Calculated spatial resolutions for various aperture diameters at  $\lambda = 633$  nm

To discuss the resolution attainable using the NSOM with a tiny aperture, we compare the results of the computational calculation by the FDTD method with the experimental results obtained by the fluorescence imaging of single molecules. The same spatial resolutions as small as 20 nm were obtained experimentally at the different excitation wavelengths ( $\lambda = 532$  and 633 nm) using the same aperture probe. The result does not agree with the results of the computational calculation for various excitation wavelengths in which about 10 nm of difference is predicted between the resolutions for the wavelengths of 532 and 633 nm. The dependence of the calculation results on the aperture sizes indicates that our computational simulation also does not reproduce the best resolutions in our measurements as high as 10 nm realized at excitations of both  $\lambda = 532$  and 633 nm. The profile of intensity distribution of fluorescence signal obtained in the experimental operations is also greatly different from that evaluated along the  $x$ -axis in the computational calculation as characterized by the well-defined double peaks in Fig. 1.8. The disappearance of the double peaks can be explained by some distortion of the aperture shape. A slight inclination of the aperture face also results in contribution of a single peak because the intensity of the other peak decreases rapidly with the distance from aperture face. Taking account of the value of the FWHM of the intensity profile for one of the double peaks in Fig. 1.8, the experimental resolution as high as 10 nm is attributed to the efficient use of the localized near-field light with a single peak profile at the rim of the aperture.

## 1.4 Single Quantum Dot Spectroscopy and Imaging

In order to evaluate optical properties of QDs, such as an extremely sharp PL line, a macroscopic measurement, where an ensemble of QDs is observed at a time, is insufficient. This is because inhomogeneous broadening is inherent to QDs due to the distribution of their sizes and shapes. Thus, the intrinsic natures are hidden in

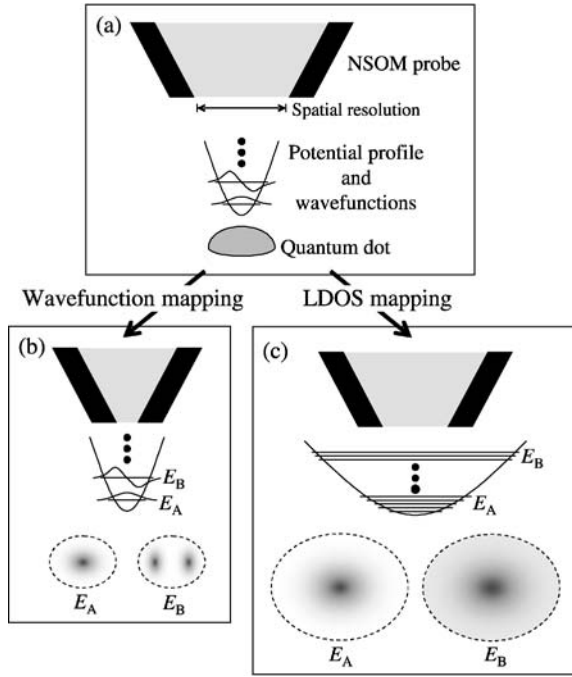


**Fig. 1.11.** Conceptual illustration of wavefunction mapping and LDOS mapping in single QD spectroscopy

an inhomogeneously broadened signal and spectroscopy on a single QD is strongly required. An NSOM offers a high spatial resolution, typically 100–200 nm, which is comparable to a typical dot-to-dot separation, and allows us to optically address individual quantum dots as illustrated in Fig. 1.11(a).

As described earlier, the size of light spot created by the NSOM probe is usually larger than the size of QD. Recent progress in the fabrication of aperture near-field fiber probe has pushed the spatial resolution to less than 30 nm [22, 25], which is comparable to or below the sizes of QDs. In such a case, NSOM allows us to investigate the inside of the QD. Roughly speaking, if the size of QD is smaller than 100 nm and the energy separation of discrete quantum levels is greater than the thermal energy at a cryogenic temperature, NSOM can visualize the spatial profile of a single quantum state: real-space mapping of an electron wavefunction [26–28]. This situation is illustrated in Fig. 1.11(b). Moreover, illumination of QD with an extremely narrow light source makes it possible to excite optically “dark” states whose excitation is forbidden by symmetry in the far field (breakdown of the usual optical selection rules) [10, 29]. These interesting observations and manipulation of electronic states in quantum confinement systems are unique to light–matter interaction at the nanoscale and the essential motivation for using the near-field optical method.

In another case we deal with a QD created by means of a nanofabrication technique. In contrast to naturally grown QDs, the size of artificially fabricated QDs can

be as large as several hundreds of nm. In such a weakly localized electron systems, where energy separation of quantized states is smaller than thermal energy, NSOM maps out the local density of states as shown in Fig. 1.11(c). Spatially and energetically resolved spectroscopy is a powerful tool to reveal the localized and delocalized electron systems and, more importantly, their crossover region (weakly localized system).

## 1.5 NSOM Spectroscopy of Single Quantum Dots

### 1.5.1 Type II Quantum Dot

A self-assembled quantum dot is an ideal system for studying zero-dimensional quantum effects and has the potential for realizing future quantum devices. In self-assembled In(Ga)As/GaAs QDs with a band alignment classified as type I, both electrons and holes are confined in the QD. In a staggered type II band structure, the lowest energy states for an electron and a hole are concentrated on different layers [30–34]. Spatial separation occurs between the electron wavefunction in the GaAs layer and the hole wavefunction in a type II GaSb QD, and the optical properties differ from those of a type I QD [30, 32].

Single QD PL spectroscopy allows us to study multiexciton states by creating many excitons in a QD under high excitation conditions [35]. The two-exciton state is an especially interesting system, because it easily forms a bound biexciton state due to the attractive Coulomb interaction in a type II In(Ga)As QD [36, 37]. The energy level of a bound biexciton state is lowered by the binding energy from the two excitons, where the binding energy is defined as the downward shift in energy of the biexciton relative to that of two uncorrelated excitons. As the stability of the biexciton state is sensitive to the structural and electronic parameters [38], the interaction between excitons in a type II GaSb QD should be different from that in a type II In(Ga)As QD. Here we describe an experimental study of the exciton and two-exciton states in a single type II GaSb QD using the NSOM.

### 1.5.2 NSOM Spectroscopy of Single GaSb QDs

The sample in this study was self-assembled GaSb QDs grown on a GaAs (100) substrate using molecular beam epitaxy [39]. The lateral size, height and density of the GaSb QDs of an uncovered sample were 16–26 nm, 5–8 nm and  $2 \times 10^{10} \text{ cm}^{-2}$ , respectively, as measured by an atomic force microscope. Cross-sectional transmission electron microscopy showed that a GaSb QD has a lens shape after capping with a GaAs cover layer of 100 nm. The sample was illuminated through the aperture with a diode laser (=685 nm) and the PL from a GaSb QD was collected via the same aperture. The PL signal was detected using a 32-cm monochromator equipped with a cooled charge-coupled device with a spectral resolution of 250  $\mu\text{eV}$ . All measurements were conducted at cryogenic temperature.

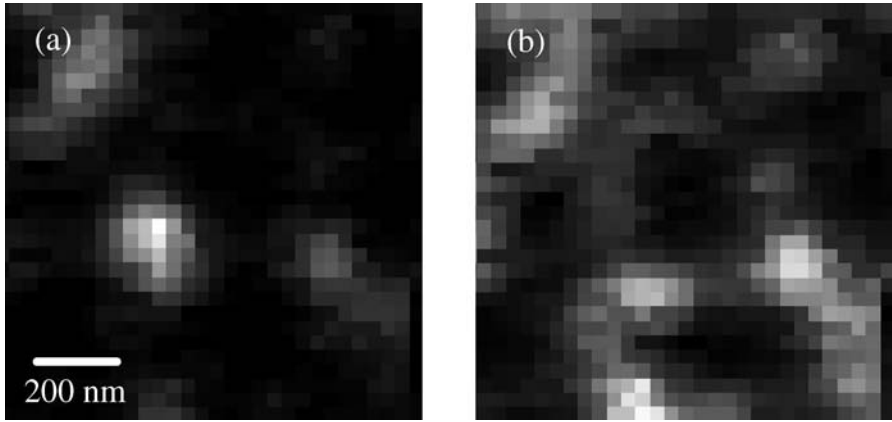
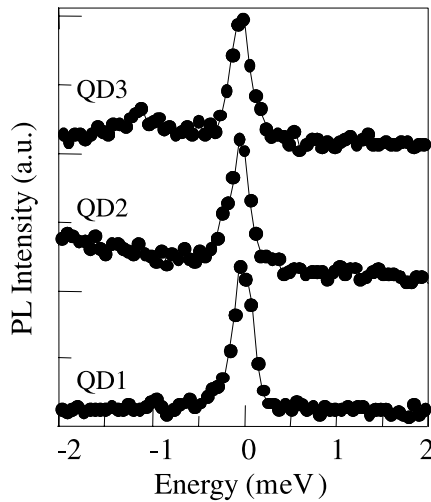


**Fig. 1.12.** Near-field PL images of single GaSb QDs monitored at photon energies of **a** 1.266 and **b** 1.259 eV, respectively

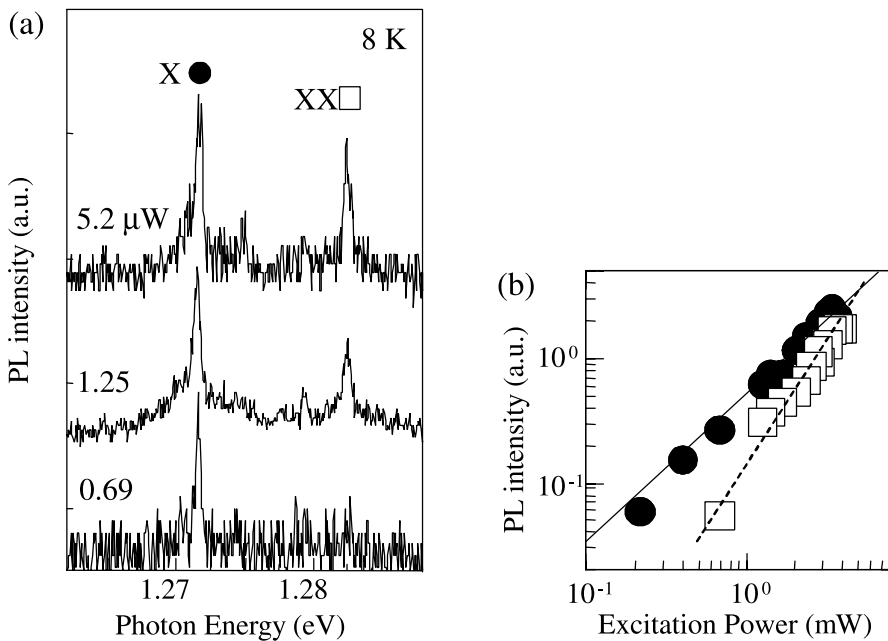
Figures 1.12(a) and 1.12(b) show typical near-field PL images, monitored at photon energies of 1.266 and 1.259 eV, respectively, under relatively low excitation conditions. Several bright spots of the PL signals from single GaSb QDs are observed in both images. We can confirm the spectroscopic observation of a single GaSb QD from the PL images. The average size of the bright spots, defined by the full width at half maximum (FWHM) of the PL intensity profile, is estimated to be about 120 nm, a value that corresponds to the spatial resolution of the measurement. The spatial resolution is somewhat larger than the aperture diameter of the probe tip (80 nm), because the GaSb QDs are embedded at a depth of 100 nm from the sample surface.

Figure 1.13 shows typical near-field PL spectra of the exciton emission from three different single GaSb QDs on an expanded energy scale. The linewidths of the three emission peaks are estimated to be  $250 \mu\text{eV}$ , where the value is limited by the spectral resolution of the measurements. Consequently, the homogeneous linewidth of an exciton state in a type II GaSb QD is evaluated to be less than  $250 \mu\text{eV}$ , which is narrower than the  $280 \mu\text{eV}$  theoretically predicted in an ideal quantum well (QW) at 8 K. The narrow PL linewidth means that the exciton state in a type II GaSb QD has a longer coherence time than that in the QW.

Figure 1.14(a) shows near-field PL spectra of a single GaSb QD at various excitation power densities. A single emission peak in the PL spectrum, denoted as X, is observed at 1.2716 eV under lower excitation conditions (less than  $1 \mu\text{W}$ ). As shown in Fig. 1.14(b), the PL intensities of the X line, as a function of excitation power densities, show an almost linear power dependence under lower excitation conditions. The sharp, less than 1 meV FWHM linewidth, X emission line is assigned to the radiative recombination of the exciton consisting of a hole confined in a GaSb QD and an electron in the surrounding GaAs barrier layer, which are weakly bound together by an attractive Coulomb interaction.



**Fig. 1.13.** PL spectra of three different single GaSb QDs at 8 K



**Fig. 1.14. a** Near-field PL spectra of a single GaSb QD at 8 K under various excitation power densities. The PL peaks at 1.2716 and 1.2824 eV are denoted as X and XX, respectively. **b** Excitation power dependence of PL intensities of the X and XX lines. The *solid (dotted) line* corresponds to the gradient associated with linear (quadratic) power dependence

Next, in Fig. 1.14(a), we focus on the PL spectra at higher excitation conditions (greater than  $1\ \mu\text{W}$ ). An additional peak appears at  $1.2824\ \text{eV}$  in the PL spectra, and the peak denoted as XX is observed at about  $11\ \text{meV}$  higher energy than the exciton emission (X). Figure 1.14(b) shows a nearly quadratic power dependence of the XX line as a function of the excitation power. The power dependence of the PL intensity suggests that the XX emission results from the radiative transition from a two-exciton state to the exciton ground state. In type I self-assembled In(Ga)As QDs [36] and naturally occurring GaAs QDs [37], the PL line is usually observed at  $3\text{--}5\ \text{meV}$  to the lower energy side of the exciton emission with the quadratic power dependence generally assigned to the bound biexciton emission. This experimental result, with the two-exciton emission occurring on the higher energy side of the exciton emission, contrasts the results in type I QDs. This is consistent with the results of the macroscopic PL spectra from GaSb QD ensembles showing a blueshift of the PL peak with increasing excitation power [30, 33].

The energy difference between the two-exciton emission (XX) and the exciton emission (X) corresponds to the binding energy ( $E_{\text{bin}} = 2E_{\text{X}} - E_{\text{XX}}$ ), where  $E_{\text{XX}}$  and  $E_{\text{X}}$  are the energy of the two-exciton state and the exciton ground state, respectively. After measuring many GaSb QDs in the same sample, we found that  $E_{\text{bin}}$  always has negative values, ranging from  $-11$  to  $-21\ \text{meV}$ . A negative  $E_{\text{bin}}$  implies that the sign of the exciton–exciton interaction is repulsive in these QDs. In type II GaSb QDs, only the holes are confined inside the QD, while the electron wave function is relatively delocalized in the GaAs barrier layer around the QDs. Consequently, it is reasonable to expect the Coulomb energy of the two-exciton ground state to be mainly dominated by the hole–hole repulsive Coulomb interaction, and to have a negative value, because the strengths of the electron–hole and electron–electron interactions are smaller than that of the hole–hole interaction.

For a quantitatively accurate understanding, we performed theoretical calculations of two-exciton states in these QDs. We used the empirical pseudopotential model (EPM) that has been applied to various III–V type I QDs [40]. The single particle states are obtained by solving the one-electron Schrödinger equation in a potential, which is obtained from the superposition of atomic pseudopotentials centered at the location of each atom in a supercell containing the QD and the surrounding matrix. Spin–orbit coupling is included as a similar sum of nonlocal potentials [40]. The EPM parameters fitted to the bulk band structure parameters of GaSb and GaAs were taken from [41].

As described earlier, the exciton and two-exciton states involve electrons weakly bound to the QD solely by the Coulomb attraction of the confined holes. This situation makes it practically impossible to calculate the exciton and two-exciton states using the conventional configuration interaction approach typically used in type I QD calculations. To handle this situation, we developed a self-consistent mean field (SCF) calculation method for multiple electron–hole pair excitations within the EPM framework. In this approach, each single particle state of a multiexciton complex is calculated by including the Coulomb potential due to all the other particles occupying the lowest possible single particle orbitals. We use Resta’s model [42] for the nonlocal dielectric constant. Our approach treats the electron–electron and electron–



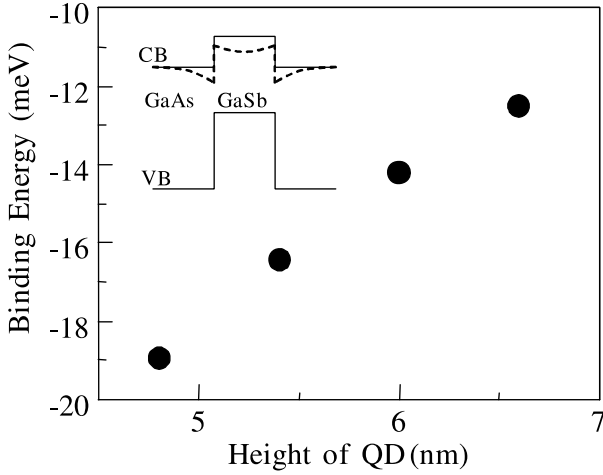


**Fig. 1.15.** Calculated biexciton binding energy as a function of the height of the lens shaped GaSb QDs. The height-to-diameter ratio was fixed as 0.3. The inset shows a schematic of the conduction band (CB) and valence band (VB) lineup of the GaSb/GaAs QDs. The dashed lines schematically illustrate the potential sensed by an electron when a hole is present

hole interactions at the Hartree–Fock level for one-exciton and two-exciton ground states and is identical to Hartree with a self-interaction correction for three or more exciton complexes.

First, we calculated the single particle energies and orbitals for a few lowest conduction and highest valence band states with zero, one and two electron–hole pairs using a linear combination of bulk Bloch functions as the basis [43]. The single- and two-exciton calculations are iterated to self-consistency. The exciton and two-exciton (biexciton) energies are calculated as the sum of single-particle energies corrected for double counting of the Coulomb interaction. A negative  $E_{\text{bin}}$  indicates that the two-exciton emission in PL spectra appears on the higher energy side of the exciton emission.

Although the structure is grown as nominally pure GaSb QDs in GaAs, independent studies have shown that relatively strong admixing of Sb and As atoms is expected [43]. Calculations were done for the lens-shaped  $\text{GaSb}_{1-x}\text{As}_x$  QDs in a GaAs matrix. The absolute exciton energies depend strongly on the alloying, as well as the size and shape of the QDs. In addition, PL studies of GaSb/GaAs type II heterostructures tell us that the observed emission energies can be explained only by using a much smaller valence offset than is theoretically accepted [44]. Therefore, it is difficult to correlate the absolute exciton energies with the experiment. The calculated  $E_{\text{bin}}$  as a function of QD size is shown in Fig. 1.15. The calculated data correspond to QDs of heights ranging from 4.8–6.6 nm with the height-to-diameter ratio fixed at 0.3. We found  $E_{\text{bin}}$  from  $-12$  to  $-19$  meV, i.e., negative values for the entire range of QD sizes considered. The range of experimentally observed binding energies is very consistent with the calculated results. A detailed analysis of

the results shows that although the two-exciton energy shift relative to the exciton could be understood qualitatively as due to the repulsion between the two confined holes, the contributions from electron–hole attraction and electron–electron repulsion are not negligible. For example, for a 4.8-nm high QD, the  $E_{\text{bin}}$  of  $-19$  meV includes  $-27$  meV of hole–hole repulsion,  $-5$  meV of electron–electron repulsion, and  $+12$  meV of electron–hole attraction.

## 1.6 Real-Space Mapping of Electron Wavefunction

With the recent progress in the nanostructuring of semiconductor materials and in the applications of these nanostructured materials in optoelectronics, NSOM microscopy and spectroscopy have become important tools for determining the local optical properties of these structures. In single quantum constituent spectroscopy, NSOM provides access to individual quantum constituent, such as QD, an ensemble of which exhibits inhomogeneous broadening due to the distribution of sizes, shapes and strains. NSOM can thus elucidate the nature of QD, including the narrow optical transition arising from the atom-like discrete density of states.

Single QD spectroscopy has revealed their long coherence times at low temperature and large oscillator strengths of optical transition. However, to improve these parameters for implementation of quantum computers, accurate information on the wavefunction for individual QDs is of great importance. In addition, in the study of coupled-QDs systems as interacting qubits, in which it is difficult to predict the exact wavefunction within theoretical frameworks, an optical spectroscopic technique for probing the wavefunction itself should be developed. By enhancing the spatial resolution of NSOM up to 10–30 nm, which is smaller than the typical size of QDs, local probing allows direct mapping of the real space distribution of the quantum eigenstate (wavefunction) within a QD, as predicted by theoretical studies [26–28].

In contrast to the well-defined quantum confined systems like QDs, the more common disordered systems with local potential fluctuations still leave open questions. To fully understand such complicated systems, exciton wavefunctions should be visualized with an extremely high resolution less than the spatial extension of wavefunction. NSOM, with a spatial resolution of 10 nm, is the only tool to obtain such information.

### 1.6.1 Light–Matter Interaction at the Nanoscale

In this section we summarize a theoretical approach to understand the light–matter interaction at the nanoscale [45]. When the nanoscale confined electron system, such as a semiconductor QD, is excited by light with a frequency  $\omega$ , the absorbed power  $\alpha(\omega)$  is

$$\alpha(\omega) \propto \int_E(\mathbf{r})P(\mathbf{r}, \omega) d\mathbf{r}, \quad (1.1)$$

where  $E(\mathbf{r})$  is the spatial distribution of electromagnetic field and  $P(\mathbf{r}, \omega)$  is the induced interband polarization. In the general form the relationship between  $P(\mathbf{r}, \omega)$

and  $E(\mathbf{r})$  should be expressed by the nonlocal electrical susceptibility  $\chi(\mathbf{r}, \mathbf{r}'; \omega)$  as

$$P(\mathbf{r}, \omega) = \int \chi(\mathbf{r}, \mathbf{r}'; \omega) E(\mathbf{r}') d\mathbf{r}', \quad (1.2)$$

$\chi(\mathbf{r}, \mathbf{r}'; \omega)$  can be obtained by eigenfunction  $\psi_{\text{ex}}$  and eigenenergy  $E_{\text{ex}}$  of exciton state confined in a QD:

$$\chi(\mathbf{r}, \mathbf{r}'; \omega) \propto \frac{\psi_{\text{ex}}(\mathbf{r}) \psi_{\text{ex}}^*(\mathbf{r}')}{E - \hbar\omega - i\gamma}. \quad (1.3)$$

Here we assume that quasi-resonant excitation at  $E_{\text{ex}}$  and therefore the contribution of other quantized exciton states are negligible.  $\gamma$  is a damping constant due to phonon scattering and radiative decay of exciton. By using (1.2) and (1.3),  $\alpha(\omega)$  can be written in the form

$$\alpha(\omega) \propto \frac{|\int \psi_{\text{ex}}(\mathbf{r}) E(\mathbf{r}) d\mathbf{r}|^2}{E - \hbar\omega - i\gamma}. \quad (1.4)$$

To illustrate the physical meaning in (1.4), we discuss two limiting cases. For far-field excitation, where QD is illuminated by a spatially homogeneous electromagnetic field,  $\alpha(\omega)$  is given by the spatial integration of the exciton wavefunction,

$$\alpha(\omega) \propto \left| \int \psi_{\text{ex}}(\mathbf{r}) d\mathbf{r} \right|^2. \quad (1.5)$$

From the value of this integral, so-called optical selection rules are derived. If the integral is zero, the corresponding transition is “forbidden” and the exciton state is optically “dark”. In the opposite limit of extremely confined light,  $E(\mathbf{r})$  is assumed to be  $\delta(\mathbf{r} - \mathbf{R})$ , where  $\mathbf{R}$  is the position of the nanoscale light source, say a near-field tip. As a result one can probe the local value of the exciton wavefunction,

$$\alpha(\omega) \propto |\psi_{\text{ex}}(\mathbf{R})|^2. \quad (1.6)$$

By measuring  $\alpha(\omega)$  as a function of the tip position, we can map out the excitation wavefunction. More interestingly, the dark-state exciton becomes visible by breaking the selection rule of optical transition. In the intermediate regime in terms of the confinement of light,  $\psi_{\text{ex}}$  are averaged over an illumination region.

Now we try to give an intuitive explanation on the local optical excitation using a classical coupled oscillator model as shown in Fig. 1.16. Each pendulum represents a localized dipole, such as a constituent molecule that makes up a molecular crystal. The dipole–dipole interaction, which forms an exciton as a collective excitation of constituent molecules, is taken into account by introducing springs to couple neighboring pendulums. Here we assume the size of the system (the size of molecular crystal) is much smaller than the wavelength of light. Figures 1.16(a) and 1.16(b) illustrate the lowest and the second lowest normal modes of the coupled oscillator, respectively. For the far-field illumination, all the pendulums are swung together at the frequency of irradiated light with the same phases. Therefore the second lowest mode, where two halves of pendulums move opposite, cannot be excited by the far-

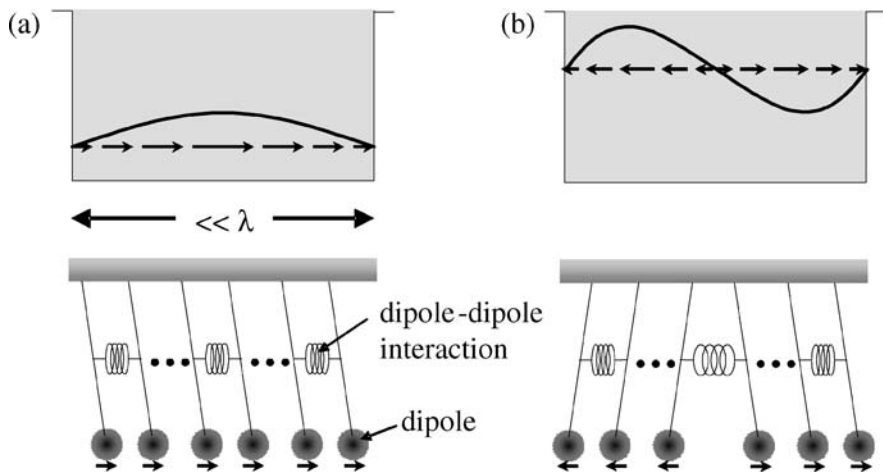


**Fig. 1.16.** Coupled pendulum model to intuitively explain the light–matter interaction at the nanoscale. **a** The lowest mode and **b** the second lowest mode of the coupled oscillator

field light whereas the lowest mode can be. This corresponds to the optical selection rule for far-field excitation of confined exciton systems. For the near-field regime, on the other hand, the situation drastically changes. The trick that the nanoscale confined light plays is to grasp solely a single pendulum and swing it. In this case, if the light frequency matches eigenfrequency of the individual oscillation mode, any normal mode can be excited regardless of the symmetry of oscillation, which means that the optical selection rule is broken by the near-field excitation. The efficiency of mode excitation is dependent on which pendulum is swung, i.e., the position of nanoscale light source. By swinging a pendulum in order from the end and observing the magnitude of mode oscillation for each we can map out the distribution of oscillation amplitude of individual pendulums. This illustrates the principle of the wavefunction mapping of exciton states.

### 1.6.2 Interface Fluctuation QD

Here we describe PL imaging spectroscopy of a GaAs QD by NSOM with a spatial resolution of 30 nm. This unprecedented high spatial resolution relative to the size of the QD (100 nm) permits a real-space mapping of the center-of-mass wavefunction of an exciton confined in the QD based on the principle discussed earlier [11, 46].

A schematic of QD sample structure is shown in Fig. 1.17. We prepared a 5-nm thick GaAs QW, sandwiched between layers of Al(Ga)As grown by molecular-beam epitaxy. Two-minute interruptions of the growth process at both interfaces lead to the formation of large monolayer-high islands which localize excitons in QD-like potential with lateral dimensions on the order of 40–100 nm [4]. The GaAs QW layer was covered with a thin barrier and a cap layer of totally 20 nm, allows the near-field tip to be close enough to the emission source (QD).

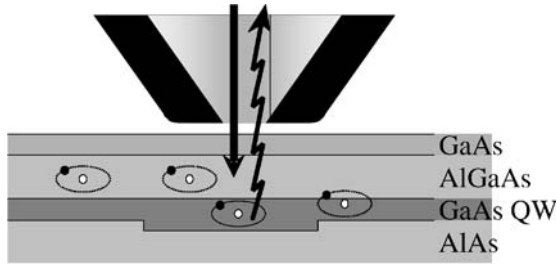


**Fig. 1.17.** A schematic of a GaAs quantum dot naturally formed in a quantum well due to the fluctuation of well thickness

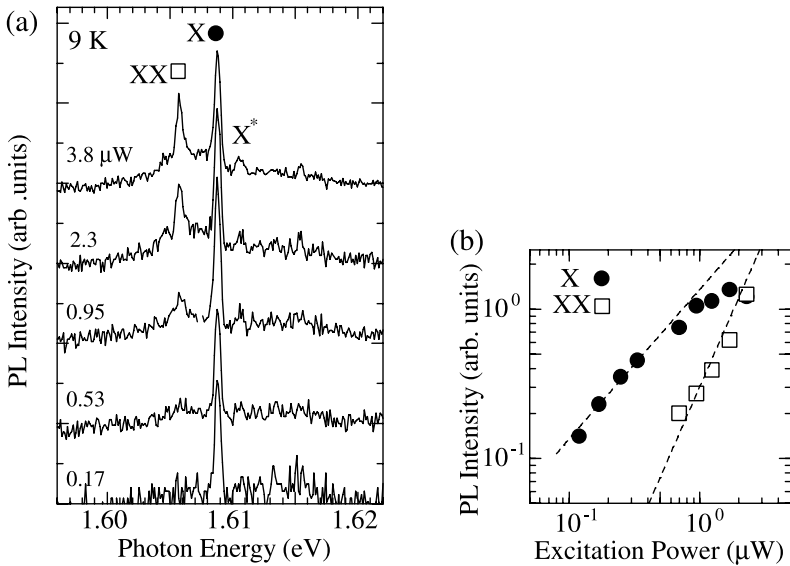


**Fig. 1.18.** **a** Near-field PL spectra of a single QD at 9 K for various excitation densities. The PL peaks at 1.6088, 1.6057 and 1.6104 eV are denoted by X, XX and X\*. **b** Excitation power dependence of PL intensities of the X and the XX lines. The two dotted lines corresponds to the gradient associated with linear and quadratic power dependence

The GaAs QD was excited with He–Ne laser light ( $\lambda = 633$  nm) through the aperture and carriers (excitons) were created in the barrier layers as well as the QW layer. Excitons diffused over several hundreds of nm and relaxed into the QDs. The PL signal from the QD was collected via the same aperture to prevent a reduction of the spatial resolution due to carrier diffusion. Near-field PL spectra were measured, for example, at 11 nm steps across a  $210 \text{ nm} \times 210 \text{ nm}$  area and two-dimensional images were constructed from a series of PL spectra.

Figure 1.18(a) shows near-field PL spectra of a single QD at 9 K at excitation densities ranging from 0.17 to  $3.8 \text{ } \mu\text{W}$ . At low excitation densities, a single emission line (denoted by X) at 1.6088 eV is observed. With an increase in excitation density,

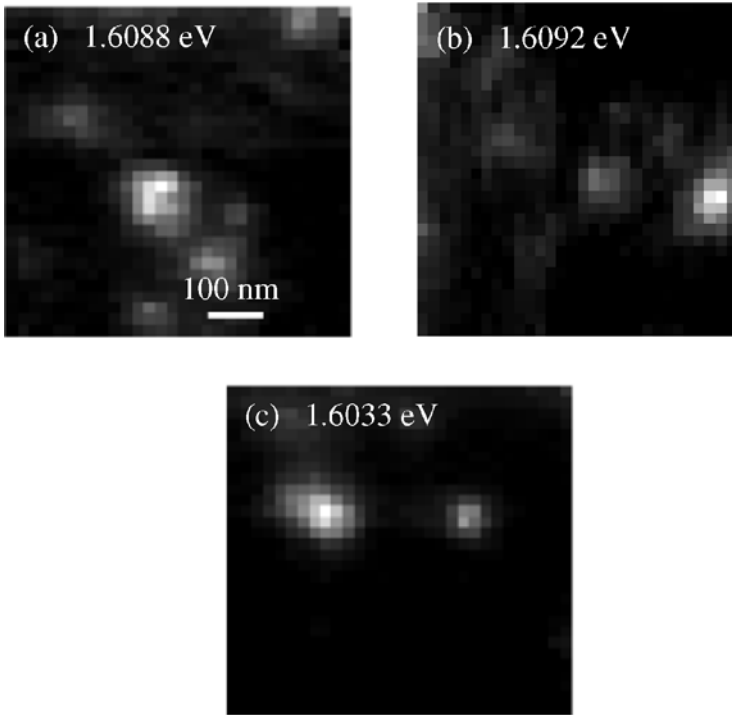


**Fig. 1.19.** Two-dimensional mapping of the PL intensity for three different X lines

the other emission lines appear at 1.6057 eV (XX) and at 1.6104 eV ( $X^*$ ). In order to clarify the origin of these emissions, we examined excitation power dependence of PL intensities as shown in Fig. 1.18(b). The X line can be identified as an emission from a single-exciton state by its linear increase in emission intensity and its saturation behavior. The quadratic dependence of the XX emission with excitation power indicates that XX is an emission from a biexciton state. This identification of the XX line is also supported by the difference in the emission energy of 3.1 meV, which corresponds to the binding energy of biexciton and agrees well with the values reported previously [47]. The  $X^*$  emission line can be attributed to the radiative recombination of the exciton excited state by considering its energy position (higher energy side of the single exciton emission by about 1.6 meV) [48]. Figure 1.19 shows low-magnification PL maps for the intensity of X emissions with three different energies in the same scanning area. These emission profiles were found to differ from QD to QD.

### 1.6.3 Real-Space Mapping of Exciton Wavefunction Confined in a QD

The high-magnification PL images in Fig. 1.20 were obtained by mapping the PL intensity with respect to the X ((a), (c) and (e)) and the XX ((b), (d) and (f)) lines of

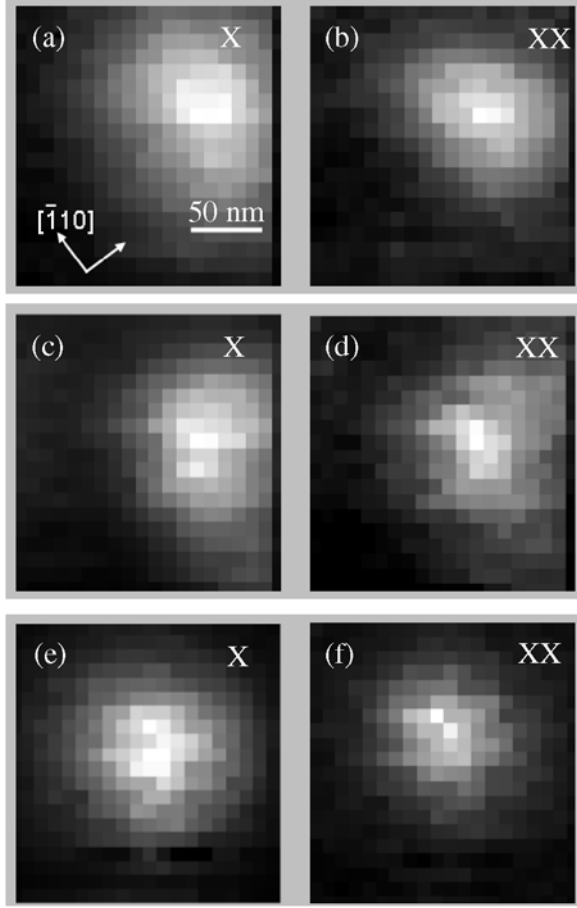


**Fig. 1.20.** Series of high-resolution PL images of exciton (X) state (**a**, **c** and **e**) and biexciton (XX) state (**b**, **d** and **f**) for three different QDs. Crystal axes along  $[110]$  and  $[-110]$  directions are indicated

three different QDs. The exciton PL images in Fig. 1.20 ((a), (c) and (e)) show an elongation along the  $[-110]$  crystal axis. The image sizes are larger than the PL collection spot diameter, i.e., the spatial resolution of the NSOM. The elongation along the  $[-110]$  axis due to the anisotropy of the monolayer-high island is consistent with previous observations with a scanning tunneling microscope (STM) [4]. We also obtained elongated biexciton PL images along the  $[-110]$  crystal axis in Fig. 1.20 ((b), (d) and (f)) and found a clear difference in the spatial distribution between the exciton and biexciton emission. Here the significant point is that the PL image sizes of biexcitons are always smaller than those of excitons.

Figures 1.21(a) and 1.21(b) show the normalized cross-sectional PL intensity profiles of exciton (thick lines) and biexciton (thin lines) along the  $[110]$  and  $[-110]$

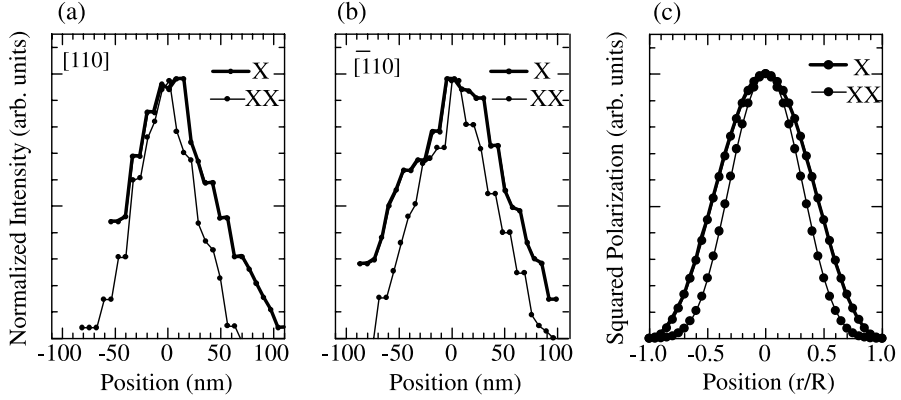


**Fig. 1.21.** High-resolution PL images and corresponding cross-sectional intensity profiles of the exciton (a and b) and the exciton excited (c and d) state. The intensity profiles are taken along *solid* and *dotted* lines in the images

crystal axes. The spreads in the exciton (biexciton) images, defined as the full width at half maximum (FWHM) of each profile are 80 (60) nm and 115 (80) nm along the  $[110]$  and  $[-110]$  crystal axes, respectively.

Theoretical considerations can clarify what we see in the exciton and biexciton PL images. The relevant quantity is the optical near-field around a single QD associated with an optical transition. This field can be calculated with Maxwell's equations using the polarization field of the exciton or biexciton as the source term. The observed luminescence intensity is proportional to the square of the near-field detected by the probe. In the following, however, we have calculated the emission patterns simply by the squared polarization fields without taking account of the instrumental details. The polarization fields at the position of the probe ( $\mathbf{r}_s$ ) are derived from the transition matrix element from the exciton state (X) to the ground state (0) and that from the biexciton state (XX) to the exciton state (X) as follows [49]:

$$\langle 0 | p \delta(\mathbf{r} - \mathbf{r}_s) | X \rangle = -\sqrt{2} p_{cv} \phi(\mathbf{r}_s, \mathbf{r}_s), \quad (1.7)$$

$$\begin{aligned} \langle X | p \delta(\mathbf{r} - \mathbf{r}_s) | XX \rangle = & -\sqrt{\frac{3}{2}} p_{cv} \sum_{\mathbf{r}_1, \mathbf{r}_a} \phi(\mathbf{r}_1, \mathbf{r}_a) \Phi^{++}(\mathbf{r}_\Delta, \mathbf{r}_s, \mathbf{r}_a, \mathbf{r}_s) \\ & - \sqrt{\frac{1}{6}} p_{cv} \sum_{\mathbf{r}_1, \mathbf{r}_a} \phi(\mathbf{r}_1, \mathbf{r}_a) \Phi^{--}(\mathbf{r}_\Delta, \mathbf{r}_s, \mathbf{r}_a, \mathbf{r}_s), \end{aligned} \quad (1.8)$$

where  $\phi(\mathbf{r}_e, \mathbf{r}_h)$  stands for the exciton envelope function with the electron and hole coordinates denoted by  $\mathbf{r}_e$  and  $\mathbf{r}_h$ ,  $\Phi^{++}(\Phi^{--})(\mathbf{r}_1, \mathbf{r}_2, \mathbf{r}_a, \mathbf{r}_b)$  represents the biexciton envelope function with electron coordinates ( $\mathbf{r}_1, \mathbf{r}_2$ ) and hole coordinates ( $\mathbf{r}_a, \mathbf{r}_b$ ) that is symmetrized (antisymmetrized) with respect to the interchange between two electrons and between two holes, and  $p_{cv}$  is the transition dipole moment between the conduction band and the valence band. The spatial distribution of the exciton polarization field corresponds to the center-of-mass envelope function of a confined



exciton. For the biexciton emission, the polarization field is determined by the overlap integral, which represents the spatial correlation between two excitons forming the biexciton and is expected to be more localized than the single exciton wavefunction.

Figure 1.21(c) shows the squared polarization amplitudes of the exciton (thick line) and biexciton (thin line) emission, which have been calculated for a GaAs QD with size parameters relevant to our experiments. The calculated profile of the squared polarization amplitude of the biexciton emission is narrower than that of the exciton emission. The spread of the biexciton emission normalized by that of the exciton emission is estimated to be 0.76, which is in good agreement with the experimental result ( $0.75 \pm 0.08$ ). This theoretical support and the experimental facts lead to the conclusion that the local optical probing by the near-field scanning optical microscope directly maps out the center-of-mass wavefunction of an exciton confined in a monolayer-high island.

Furthermore, we can demonstrate a novel powerful feature of the wavefunction mapping spectroscopy. Figure 1.22 shows the PL image and corresponding cross-sectional intensity profiles of the exciton ground state X ((a) and (b)) and the exciton excited state X\* ((c) and (d)) from a single QD, which is different from that observed in Fig. 1.21. The exciton PL image exhibits a complicated shape in this QD, unlike the simple elliptical shape shown in Fig. 1.21. This is because the exciton is confined in a monolayer-high island with an extremely anisotropic shape. The significant point is that the exciton ground state image exhibits a single maximum peak in the intensity profile, while a double-peaked intensity profile is obtained from the exciton excited state. This is attributable to the difference in spatial distribution of the center-of-mass wavefunction, which has no node in the ground state, but does have a node in the excited state.

## 1.7 Real-Space Mapping of Local Density of States

Since the local electronic structure—defined as the local density of states (LDOS) in metal corrals—was first demonstrated using scanning probe microscopy and spectroscopy [50, 51], the LDOS mapping technique has been applied to many interesting quantum systems, such as two-dimensional (2D) electron gas [52], one-dimensional quantum wires [53] and zero-dimensional (0D) quantum dots (QDs) [54]. Although NSOM is useful for studying the elementary excitation of these quantum structures with less than subwavelength spatial resolution, there are only a few results of LDOS mapping using NSOM: for example, observation of the optical LDOS of an optical corral structure with a forbidden light [55].

Here we probed the local electronic states of a Be-doped GaAs/Al<sub>1-x</sub>Ga<sub>x</sub>As single heterojunction with a surface gate using an NSOM. The spatial distribution of LDOS in a field-induced quantum structure can be mapped using near-field PL microscopy, as the quantum structure investigated here is larger than the spatial resolution of NSOM and the PL spectrum reflects the DOS of electrons.

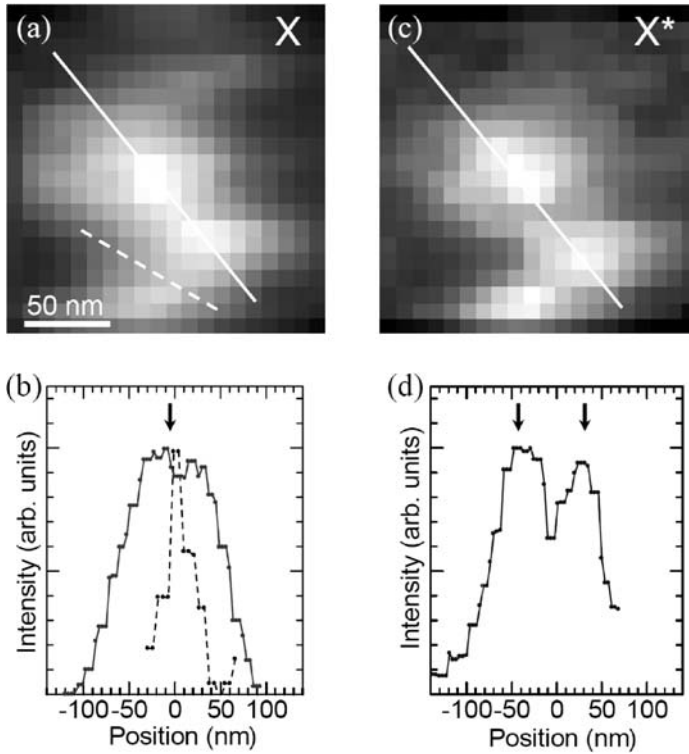


**Fig. 1.22.** **a, b** Normalized cross-sectional intensity profiles of exciton (thick lines) and biexciton (thin lines) PL images corresponding to Figs. 1.20(a) and (b). **c** Spatial distributions of squared polarization fields of the exciton (thick line) and biexciton (thin line) emission, which are theoretically calculated for a GaAs quantum dot (radius of 114 nm, thickness of 5 nm). The horizontal axis is normalized by the disk radius  $R$

### 1.7.1 Field-Induced Quantum Dot

The QDs formed by an electrostatic field effect have been extensively studied [56–59]. In a field-induced QD, the strength and lateral profile of the confinement potential can be tuned using the design of the surface gate and the strength of the bias-voltage applied to the surface gate. As the degradation and imperfections at interfaces are minimized owing to electrostatic confinement, the electrons are confined by the well-defined lateral potential in this system. The properties of confined electrons have been investigated using macroscopic PL spectroscopy in a field-induced quantum structure based on a Be-doped single heterojunction [59, 60]. In this characteristic structure, the PL spectrum arising from the recombination of holes bound to Be acceptors with electrons in an electron gas provides us with a probe to investigate the DOS of electrons owing to relaxation of the  $k$ -selection rule in the optical process [59, 61, 62].

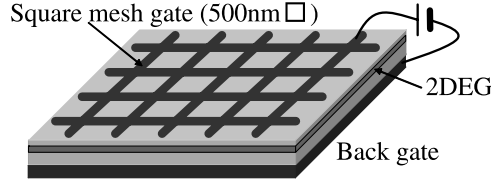


**Fig. 1.23.** A schematic of AlGaAs/GaAs two-dimensional electron gas with a mesh gate structure

The sample investigated in this study was a Be-doped single heterojunction of a GaAs/Al<sub>1-x</sub>Ga<sub>x</sub>As ( $x = 0.7$ ) structure fabricated using molecular beam epitaxy [59, 62]. Figure 1.23 illustrates a rough schematic of sample structure. The heterostructure was grown on an n-type GaAs substrate used as the back contact and was fabricated under 75 nm from the surface. The nominal concentration of Be dopant was  $2.0 \times 10^{10} \text{ cm}^{-2}$  and the Be-doped layer was inserted 25 nm below the heterojunction interface. The estimated sheet electron density without modulation using an external bias-voltage ( $V_B$ ) was  $3.6 \times 10^{11} \text{ cm}^{-2}$  at 1.8 K, using an optical Shubnikov–de Hass measurement. A semitransparent Ti/Au Schottky gate structure on the surface was fabricated with a square mesh of a 500-nm period using electron beam lithography. The bias-voltage was applied between the surface Schottky gate and the Ohmic back electrode.

An aperture about 120 nm in diameter was fabricated by milling of the probe apex using a focused ion beam (FIB) apparatus. The sample on the scanning stage was illuminated with a cw diode laser light ( $\lambda = 685 \text{ nm}$ ) through the aperture, and a time-integrated PL signal from the sample was collected via the same aperture. The PL signal was sent to a 32-cm monochromator with a cooled charge coupled device with a spectral resolution of  $220 \mu\text{eV}$ . The spatial resolution of NSOM in this study was about 140 nm.

Figure 1.24 shows far-field PL spectra, measured at the  $V_B$  ranging from 0 to  $-1.6 \text{ V}$ . The PL signal from the 1.475 to 1.491 eV region is attributed to the recombination between the localized holes bound to Be accepters with electrons in the electron gas. The holes bound to Be accepters can recombine with any electrons with wave vectors up to the inverse of the hole Bohr radius with nearly equal optical transition probabilities [59–62]. Owing to the small effective Bohr radius of the hole bound to the Be acceptor, the PL spectrum of the 1.475–1.491 eV region reflecting the DOS of electrons [59] is used as a probe to investigate the electronic structure. Under low negative bias conditions ( $V_B < -0.35 \text{ V}$ ), the signals from 1.480 to 1.489 eV show flat shape PL spectra reflecting the 2D DOS. The strong peaks at 1.496 eV come from the recombination between 2D electrons in the second subband with holes bound to the accepters [60]. When the  $V_B$  is increased to  $-1.6 \text{ V}$ , the PL spectra show a linear increase in intensity toward higher photon energies from 1.480 to 1.489 eV. This behavior is expected from the 0D DOS of electrons because the linear dependence is in accordance with the generally accepted picture, in which the degeneracy of states increases with the quantum number.

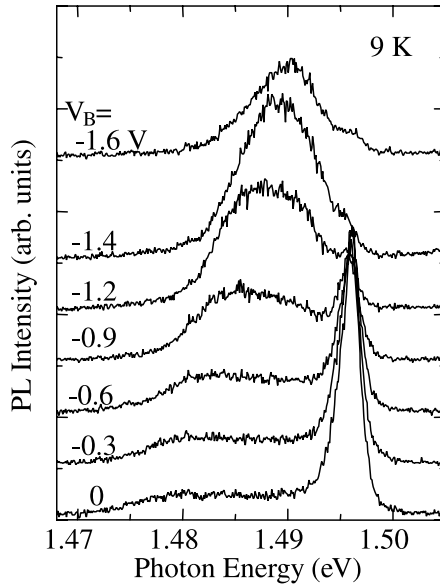


**Fig. 1.24.** Bias-voltage ( $V_B$ ) dependence of macroscopic PL spectra of a Be-doped single heterojunction

### 1.7.2 Mapping of Local Density of States in a Field Induced QD

We investigated the local electronic states of the field-induced quantum structure while tuning the external bias voltage. As the PL intensity owing to the recombination of holes with electrons in an electron gas is proportional to the amplitude of the DOS and the spatial resolution of NSOM is higher than the size of the quantum structure, we can map the LDOS experimentally by monitoring the spatial distribution of the PL intensity from 1.475 to 1.491 eV. The atomic force microscopy image of a gated sample surface in Fig. 1.25(a) shows a square mesh gate with a 500-nm period. Figures 1.25(b)–2(e) show near-field optical images obtained by detecting the PL intensity at around 1.483 eV while changing the external bias-voltage ( $V_B = 0, -1.2$ , and  $-1.6$  V). In a series of images, we can observe the change in the PL images from 2D (plane) to 0D (dot) features with the application of  $V_B$  to the surface gate. For  $V_B = -1.6$  V, a bright spot is observed in the center of the square mesh gate in the PL image in Fig. 1.25(d). Looking at a wide spatial area, we see an array of PL spots corresponding to the period of the square mesh, as shown in Fig. 1.25(e). The change induced by applying a bias voltage is also supported by the cross-sectional intensity profiles shown in Fig. 1.25(f), taken along a diagonal of the mesh gate at the same positions. The size of the full width at half maximum (FWHM) of the profiles decreases from 400 nm at  $V_B = 0$  V to 160 nm at  $V_B = -1.6$  V. The narrow distribution of the PL intensity is caused by depletion of the electron density in the electron gas around the mesh gate under the external bias voltage. As a result, there is a dense electron population at positions far from the mesh gate and the potential

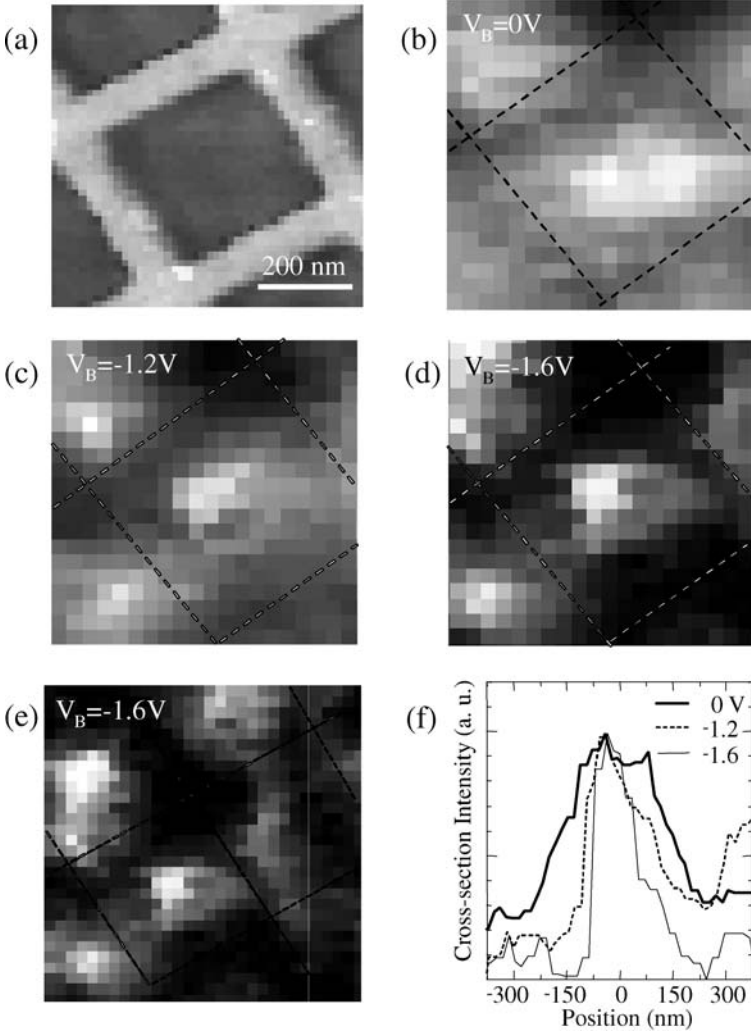


**Fig. 1.25.** **a** Shear-force microscopy (topographic) image of the gated sample surface (height contrast: 50 nm). **b–d** Near-field PL images at different bias voltages  $V_B = 0$ ,  $-1.2$ , and  $-1.6$  V, respectively. These images were monitored at a detection energy of around 1.483 eV at 9 K. The dotted lines in the images correspond to the position of the surface gate. **e** Near-field PL image at  $V_B = -1.6$  V, measured for a wide area. **f** Cross-sectional PL intensity profiles taken along a diagonal of the mesh gate

for electrons is minimal at the center of the mesh gate. Therefore, the change in the PL image directly connects to the change in electronic structure from a 2D electron gas to the confined 0D electronic state (QD) and an artificially formed QD array, induced by the electrostatic confinement potential.

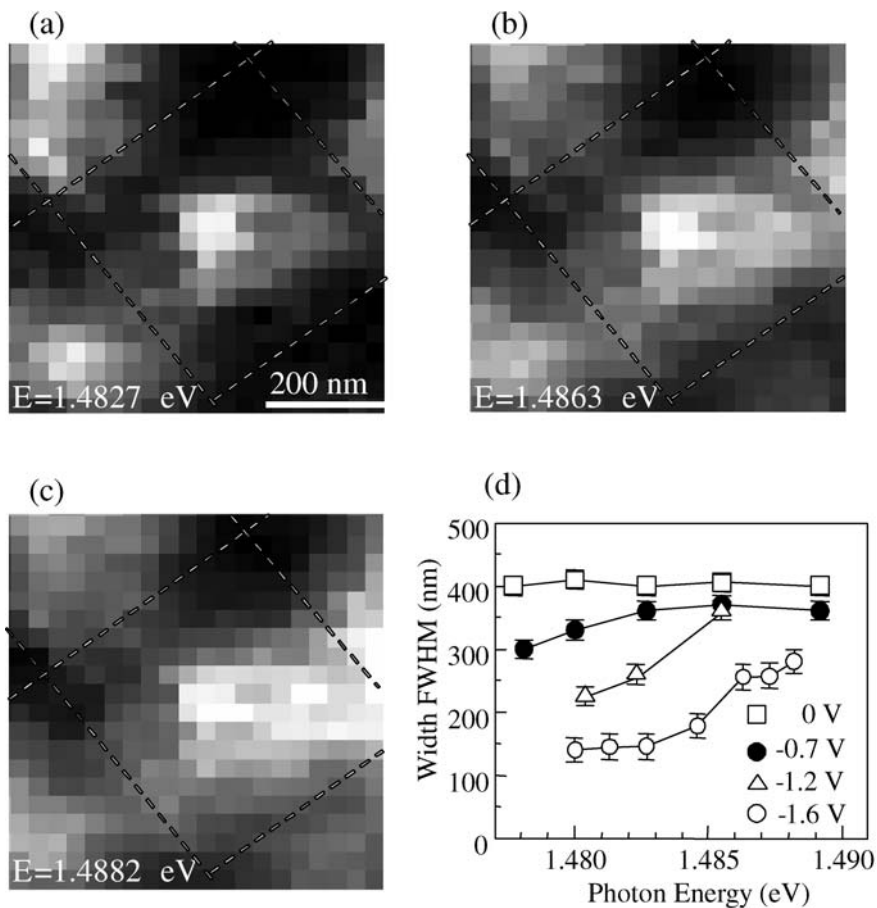


**Fig. 1.26.** **a–c** Near-field PL images obtained at different detection energies under a bias voltage of  $-1.6$  V. **d** PL intensity distribution defined as the FWHM of the profiles as a function of the detection photon energy under various bias-voltage conditions

Figures 1.26(a)–1.26(c) show PL images in the QD state under  $V_B = -1.6$  V, detected at 1.4827, 1.4863 and 1.4882 eV, respectively. The spatial distribution of the PL intensity changes with the monitored photon energy and gradually spreads, going from an image at a lower photon energy to one at a higher photon energy [from Fig. 1.26(a)–1.26(c)]. We evaluated the spread of the PL image defined as the FWHM of the intensity profile as a function of photon energy and plotted the values for various bias voltages in Fig. 1.26(d). At low bias voltage ( $-0.7$  V), the values of the spread in the PL images are essentially constant for the entire energy range from 1.477 to 1.490 eV, which is easily understood from the 2D DOS characteristics. By contrast, under higher bias voltage, the spread of the PL image strongly depends on the monitored energy and the value increases gradually toward the higher energy

side, which indicates that the distribution of the LDOS gradually spreads from lower to higher energy states in a field-induced QD.

To confirm the feasibility of the LDOS mapping, we refer the numerical calculation results of the electron density distribution derived from solving Schrödinger and Poisson's equations [62–65]. The calculated potential for electrons in this quantum structure is minimal at the center of the mesh gate with an application of the bias voltage [62, 63]. The electrons with lower energy near the bottom of the electrostatic potential are confined strictly and the spatial distribution of the wave function extends with increasing energy. The experimental results obtained from the near-field PL images are consistent with the calculated electron density distributions and its energy dependence. Thus, the optical near-field microscopy maps the LDOS in a field-induced quantum structure.

Finally, we will mention the near-field PL spectrum of a field-induced single QD (not shown here). We did not observe the sharp spectral features, as frequently observed for 0D systems (QDs) [66, 67]. A peak in the PL spectrum arising from each confined level should be broadened by at least 0.5 meV, taking into consideration the estimated energy separation between confined levels [63]. This broadening might be because it takes 0.1–1  $\mu$ s for the nonequilibrium electrons to cool after excitation [61]. Therefore, the combination of near-field PL microscopy with the time-gated PL detection technique will enable us to observe fine spectral structures of a field-induced QD.

## 1.8 Carrier Localization in Cluster States in GaNAs

### 1.8.1 Dilute Nitride Semiconductors

In contrast to the well-defined quantum confined systems such as QDs grown in a self-assembled mode, the more common disordered systems with local potential fluctuations leave unanswered questions. For example, a large reduction of the fundamental band gap in GaAs with small amounts of nitrogen is relevant to the clustering behavior of nitrogen atoms and resultant potential fluctuations [68]. NSOM characterization with high spatial resolution can give us a lot of important information that is useful in our quest to fully understand such complicated systems, such as details about the localization and delocalization of carriers, which determine the optical properties in the vicinity of the band gap.

Dilute GaNAs and GaInNAs alloys are promising materials for optical communication devices [69–71] because they exhibit large band-gap bowing parameters. In particular, for long-wavelength semiconductor laser application, high temperature stability of the threshold current is realized in the GaInNAs/GaAs quantum well as compared to the conventional InGaAsP/InP quantum well due to strong electron confinement. However, GaNAs and GaInNAs with a high nitrogen concentration of more than 1% have been successfully grown only under nonequilibrium conditions by molecular beam epitaxy and metal organic vapor phase epitaxy.

The incorporation of nitrogen generally induces degradation of optical properties. To date, several groups of researchers have reported characteristic PL properties of GaNAs and GaInNAs, for example, the broad asymmetric PL spectra and the anomalous temperature dependence of the PL peak energy. More seriously emission yield drastically degraded with an increase of nitrogen concentration.

For improvement of their fundamental optical properties, it is strongly required to clarify electronic states due to single N impurities [72, 73] or N clusters, which interact with each other and with the host states. The interaction gives rise to the formation of weakly localized and delocalized electronic states at the band edge. Hence the shape of optical spectra is extremely sensitive to the N composition. In conventional spatially resolved PL spectroscopy, it is easy to detect single impurity emissions in ultradilute compositional region. However, in order to resolve complicated spectral structures and to clarify the interaction of localized states and the onset of alloy formation, a spatial resolution far beyond the diffraction limit is needed.

Here we show the results of spatially resolved PL spectroscopy with a high spatial resolution of 30 nm. Spatial inhomogeneity of PL is direct evidence of carrier localization in the potential minimum case caused by the compositional fluctuation. PL microscopy with such a high spatial precision enables the direct optical observation of compositional fluctuations, i.e., spontaneous N clusters and N random alloy regions, which are spatially separated in  $\text{GaN}_x\text{As}_{1-x}/\text{GaAs}$  QWs.

### 1.8.2 Imaging Spectroscopy of Localized and Delocalized States

The samples investigated in this study were 5-nm thick  $\text{GaN}_x\text{As}_{1-x}/\text{GaAs}$  single QWs with different N compositions ( $x = 0.7\%$  and  $1.2\%$ ) grown on (001) GaAs substrates using low-pressure metalorganic vapor phase epitaxy [74]. The growth temperature was  $510^\circ\text{C}$  and the details of the growth conditions have been described elsewhere [74]. The GaNAs layer was sandwiched between a 200-nm thick GaAs buffer layer and a 20-nm thick GaAs barrier layer. The thin 20-nm thick barrier layer allowed a near-field probe tip to come close enough to the emission sources to achieve a spatial resolution as high as 35 nm. The N composition ( $x$ ) of the QW layer was estimated using secondary ion mass spectroscopy and cross-checked using the energy position in the PL spectra [75]. After growth, thermal annealing was performed for 10 min in a mixture of  $\text{H}_2$  and TBAs at  $670^\circ\text{C}$  to improve the PL intensity [74].

We used NSOM probe tips with apertures of different diameters (30 and 150 nm), depending on the measurements. Optical measurements were performed at 8 K with a setup similar to that described earlier. Near-field PL spectra were obtained at every 12 nm steps for a  $300\text{ nm} \times 300\text{ nm}$  area, and two-dimensional PL maps were constructed from a series of these spectra.

The dotted line in Fig. 1.27 shows a far-field PL spectrum of a single  $\text{GaN}_x\text{As}_{1-x}/\text{GaAs}$  ( $x = 0.7\%$ ) QW at low temperature. The far-field spectrum has a broad linewidth of 30 meV and a lower-energy tail. To resolve the inhomogeneously broadened PL spectrum, we carried out near-field PL measurements with a high spatial resolution of 35 nm. The near-field PL spectrum in Fig. 1.27 has fine structures that



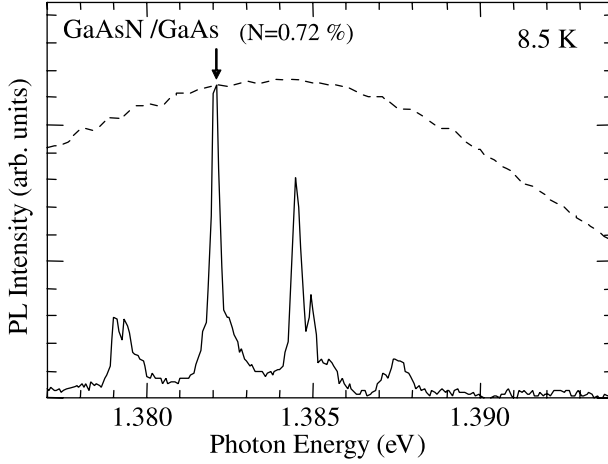


**Fig. 1.27.** Far-field (dotted line) and near-field (solid line) PL spectra of a  $\text{GaN}_x\text{As}_{1-x}/\text{GaAs}$  ( $x = 0.72\%$ ) single QW at 8.5 K

are not observed in the far-field spectrum [76–78]. After analyzing several thousands of near-field PL spectra, we found that the fine structures in the near-field PL spectra were divided into two groups: Sharp luminescence peaks with narrow linewidths below 1 meV and broad peaks with linewidths of several meV. We discuss the origin of these spectral features using both spectral and spatial information.

Figure 1.28(a) shows a typical near-field PL spectrum with sharp emission lines. To evaluate the linewidth, we show one of the sharp emission lines (1.382 eV) at an expanded energy scale in the inset; the spectral linewidth, defined as the full width at half maximum (FWHM), was determined to be less than 220  $\mu\text{eV}$ , which is limited by the spectral resolution. The narrow PL linewidth means that the exciton state has a long coherence time, i.e., there is a reduction of the scattering rate between an exciton and phonons due to the change in the electronic structures from a continuum to discrete density of states. Such discrete density of states might be explained by the formation of naturally occurring quantum dot (QD) structures in a narrow  $\text{GaN}_x\text{As}_{1-x}/\text{GaAs}$  QW ( $x = 0.7\%$ ).

The spatial characteristics of the naturally occurring QD structures in a narrow QW showing the sharp emissions should be investigated. Figure 1.28(b) shows a high-resolution optical image of the sharp PL line, obtained by mapping the intensity (denoted by the arrow in Fig. 1.27). The surface topography did not influence the optical images, because the sample had a flat surface with a roughness of less than several nm, as estimated from a shear-force topographic image. The PL image clearly shows a point-emission feature, and the spot size defined as the FWHM of the cross-sectional profile shown in Fig. 1.28(c) is estimated to be 35 nm, which is limited by the spatial resolution of NSOM. The experimental spatial and spectral results suggest that the exciton strongly localizes in a potential minimum of naturally occurring QD structure in a narrow QW. The local N-rich regions (spontaneous N clusters) in a

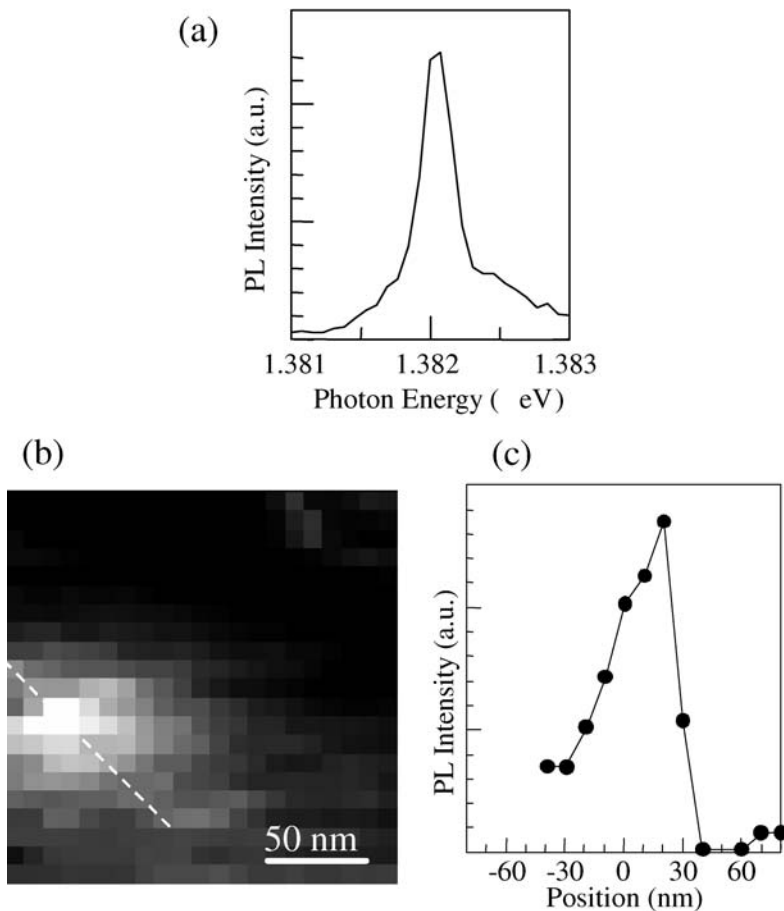


**Fig. 1.28.** **a** Near-field PL spectrum with a sharp emission peak. **b** Two-dimensional PL intensity mapping of the sharp emission line at 1.382 eV. **c** Cross-sectional PL intensity profile taken along the dotted line in **b**. The size of the emission profile, defined as the FWHM, is 35 nm (restricted by the spatial resolution of NSOM)

GaNAsN layer are the origin of the naturally occurring QD structures, as indicated by transmission electron microscopy [79].

Consider the broad peaks in the near-field PL spectrum. Figure 1.29(a) shows a typical PL spectrum of a broad peak with a 3 meV linewidth, which is much broader than below 220  $\mu\text{eV}$  for the sharp emission line. The two-dimensional PL intensity map of the broad emission line in Fig. 1.29(b) shows spatially extended behavior that extends approximately 80 nm, as estimated from the cross-sectional profile in Fig. 1.29(c) (taken along the dotted line in the PL image). These characteristics of the broad PL line indicate that the exciton has a delocalized nature due to the random alloy state, which is frequently observed in isovalent semiconductor alloys. In addi-

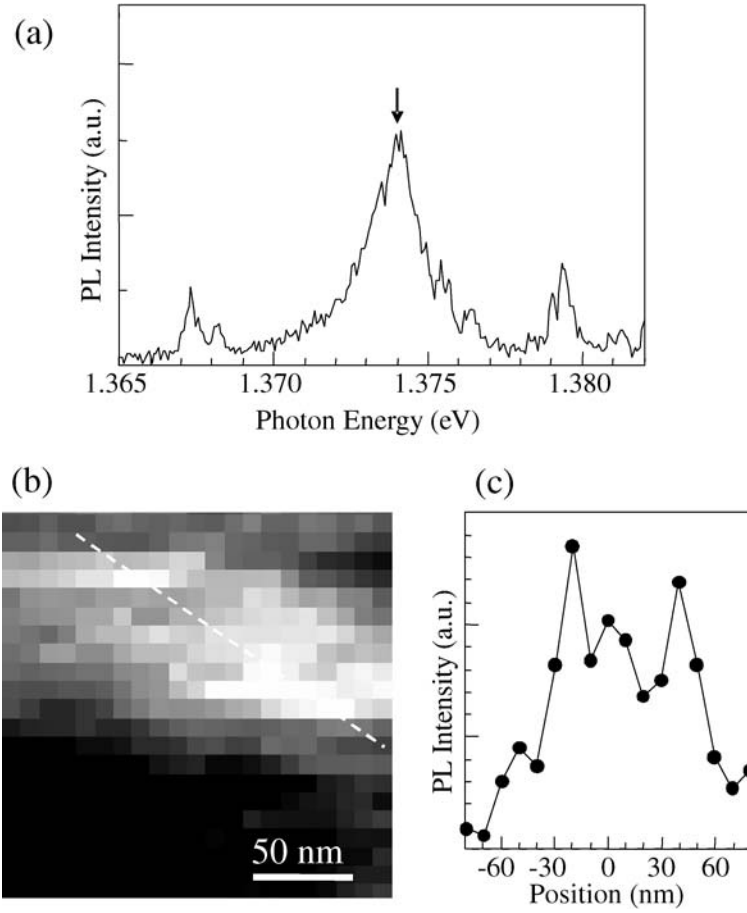


**Fig. 1.29.** **a** Near-field PL spectrum with a broad emission peak. **b** PL intensity map of the broad emission line at 1.374 eV. The scanning area is same as that of Fig. 1.1(b). **c** Cross-sectional PL intensity profile of the broad emission along the dotted line in **b**. The FWHM of the profile is 80 nm

tion, the energy positions and linewidths in the PL spectra are unchanged throughout the bright regions in Fig. 1.29(b), which supports the delocalized nature of excitons. Note that the PL images in Figs. 1.28(b) and 1.29(b) were obtained in the same scanning area. Therefore, the regions with randomly distributed N and the spontaneous N-rich clusters are separated spatially in  $\text{GaN}_x\text{As}_{1-x}$  ( $x = 0.7\%$ ), as observed directly using NSOM with a high spatial resolution of 35 nm.

We investigated the compositional fluctuations in  $\text{GaN}_x\text{As}_{1-x}$  for different concentrations of N. Figure 1.30 shows near-field PL spectra for  $x = 1.2\%$  at different spatial positions. These PL spectra were obtained using a probe tip with a 150-nm aperture, because the PL intensity strongly depends on  $x$  [77] and the intensity at

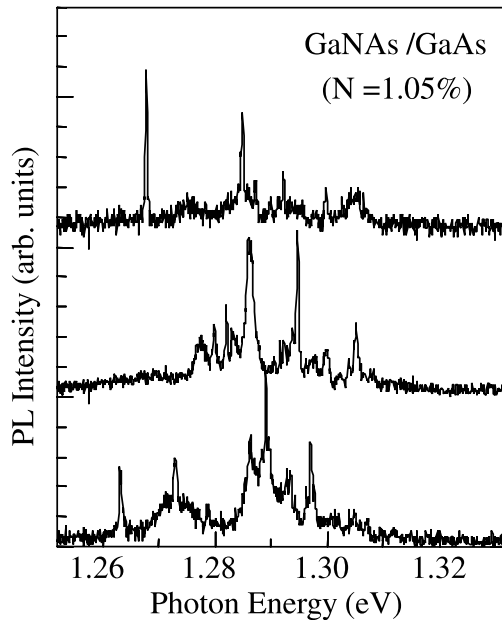


**Fig. 1.30.** Near-field PL spectra of  $\text{GaN}_x\text{As}_{1-x}/\text{GaAs}$  ( $x = 1.2\%$ ). The PL spectra measured at different positions were normalized by the maximum peak intensity

higher  $x$  ( $=1.2\%$ ) decreases by about one order of magnitude compared with that for  $x = 0.7\%$ . The near-field PL spectra in Fig. 1.30 consist of many sharp lines from localized exciton recombinations in N-rich clusters and broad emissions, similar to the near-field PL spectra for  $x = 0.7\%$ . Note that sharp emission peaks are observed in the PL spectra for  $x > 1\%$ . Recent macroscopic PL [80] and magneto-PL [77] measurements of  $\text{GaN}_x\text{As}_{1-x}$  for  $x = 1.0\%$  showed broad, smooth spectra, which were assigned to emissions from delocalized excitons. However, our near-field PL spectroscopy reveals that the inhomogeneous broadened PL spectrum consists of the sharp emission lines owing to the recombinations of excitons localized in N-rich clusters superimposed on the broad emissions from the delocalized exciton state in  $\text{GaN}_x\text{As}_{1-x}$  ( $x = 1.2\%$ ). The regions of randomly distributed N and spontaneous N-rich clusters coexist at N compositions over  $1\%$ .

## 1.9 Perspectives

The dramatic progress in the spatial resolution of near-field optical microscopes offers an exciting opportunity for the study of light–matter interaction at the nanoscale. Real-space imaging of spatial distributions of quantized states can answer fundamental questions about the localized and delocalized nature of electrons in complicated potential systems, such as disorder alloy semiconductors. Ultimately, small light spots affect the light–matter interaction through the modification of quantum

interference. This allows us to break the optical selection rule and to excite dark states.

A nanoscale light source also provides new techniques for wave packet engineering; creation, detection, transport, tailoring and coherent control of the electron wave packet. The pronounced quantum features of wave packet dynamics in nanoscale length will open new possibilities for controlling the capture processes from delocalized states to localized states. In combination with spin degree of freedom, control of spin-polarized wave packets leads to the realization of nano-spintronic devices.

## Acknowledgments

We are grateful to M. Ohtsu, S. Mononobe, K. Matsuda, N. Hosaka, M. Sakai, K. Sawada, H. Nakamura, Y. Aoyagi, M. Mihara, S. Nomura, S. Nair, T. Tagahara, M. Takahashi, A. Moto, and S. Takagishi for their assistance and fruitful discussions.

## References

- [1] Ohtsu, M., Kobayashi, K., Kawazoe, T., Sangu, S., Yatsui, T.: IEEE J. Sel. Top. Quantum Electron. **8**, 839 (2002)
- [2] P. Micheler, *Single Quantum Dots* (Springer, Berlin, 2003)
- [3] D. Gammon, E.S. Snow, B.V. Shanabrook, D.S. Katzer, D. Park, Phys. Rev. Lett. **76**, 3005 (1996)
- [4] J. Hours, P. Senellart, E. Peter, A. Cavanna, J. Bloch, Phys. Rev. B **71**, R161306 (2005)
- [5] M. Ohtsu, *Near-Field Nano/Atom Optics and Spectroscopy* (Springer, Tokyo, 1998)
- [6] L. Novotny, B. Hecht, *Principles of Nano-Optics* (Cambridge University Press, New York, 2006)
- [7] N. Hosaka, T. Saiki, Opt. Rev. **13**, 262 (2006)
- [8] J.N. Farahani, D.W. Pohl, H.-J. Eisler, B. Hecht, Phys. Rev. Lett. **95**, 17402 (2005)
- [9] K. Cho, *Optical Response of Nanostructures* (Springer, Berlin, 2003)
- [10] K. Matsuda, T. Saiki, S. Nomura, M. Mihara, Y. Aoyagi, S. Nair, T. Takagahara, Phys. Rev. Lett. **91**, 177401 (2003)
- [11] K. Karrai, R.D. Grober, Appl. Phys. Lett. **66**, 1842 (1995)
- [12] T. Saiki, K. Nishi, M. Ohtsu, Jpn. J. Appl. Phys. **37**, 1638 (1998)
- [13] H. Nakamura, T. Sato, H. Kambe, K. Sawada, T. Saiki, J. Microscopy **202**, 50 (2001)
- [14] T. Saiki, S. Mononobe, M. Ohtsu, N. Saito, J. Kusano, Appl. Phys. Lett. **68**, 2612 (1996)
- [15] D.W. Pohl, W. Denk, M. Lanz, Appl. Phys. Lett. **44**, 651 (1984)
- [16] T. Saiki, K. Matsuda, Appl. Phys. Lett. **74**, 2773 (1999)
- [17] P. Anger, P. Bharadwaj, L. Novotny, Phys. Rev. Lett. **96**, 113002 (2006)
- [18] J. Michaelis, C. Hettich, J. Mlynek, V. Sandoghdar, Nature **405**, 325 (2000)
- [19] R. Eckert, J.M. Freyland, H. Gersen, H. Heinzelmann, G. Schurmann, W. Noell, U. Staufer, N.F. de Rooij, Appl. Phys. Lett. **77**, 3695 (2000)
- [20] J.M. Kim, T. Ohtani, H. Muramatsu, Surf. Sci. **549**, 273 (2004)
- [21] N. Hosaka, T. Saiki, J. Microscopy **202**, 362 (2001)
- [22] H. Furukawa, S. Kawata, Opt. Commun. **132**, 170 (1996)
- [23] E.D. Palik, *Handbook of Optical Constants of Solids* (Academic Press, New York, 1985)

- [24] K. Matsuda, T. Saiki, S. Nomura, M. Mihara, Y. Aoyagi, Appl. Phys. Lett. **81**, 2291 (2002)
- [25] G.W. Bryant, Appl. Phys. Lett. **72**, 768 (1998)
- [26] Di Stefano, S. Savasta, G. Pistone, G. Martino, R. Girlanda, Phys. Rev. B **68**, 165329 (2003)
- [27] E. Runge, C. Lienau, Appl. Phys. B **84**, 103 (2006)
- [28] U. Hohenester, G. Goldone, E. Molinari, Phys. Rev. Lett. **95**, 216802 (2005)
- [29] F. Hatami, M. Grundmann, N.N. Ledentsov, F. Heinrichsdorff, R. Heitz, J. Bohrer, D. Bimberg, S.S. Ruvimov, P. Werner, V.M. Ustinov, P.S. Kop'ev, Zh.I. Alferov, Phys. Rev. B **57**, 4635 (1998)
- [30] K. Suzuki, R.A. Hogg, Y. Arakawa, J. Appl. Phys. **85**, 8349 (1999)
- [31] Ph. Lelong, K. Suzuki, G. Bastard, H. Sakaki, Y. Arakawa, Physica E **7**, 393 (2000)
- [32] L.M. Kirsch, R. Heitz, A. Schliwa, O. Stier, D. Bimberg, H. Kirmse, W. Neumann, Appl. Phys. Lett. **78**, 1418 (2001)
- [33] E. Ribeiro, A.O. Govorov, W. Carvalho, G. Medeiros-Ribeiro, Phys. Rev. Lett. **92**, 126402 (2004)
- [34] E. Dekel, D. Gershoni, E. Ehrenfreund, D. Spektor, J.M. Garcia, P.M. Petroff, Phys. Rev. Lett. **80**, 4991 (1998)
- [35] D.V. Regelman, U. Mizrahi, D. Gershoni, E. Ehrenfreund, W.V. Schoenfeld, P.M. Petroff, Phys. Rev. Lett. **87**, 257401 (2001)
- [36] K. Brunner, G. Abstreiter, G. Bohm, G. Trankle, G. Weimann, Phys. Rev. Lett. **73**, 1138 (1994)
- [37] S. Rodt, R. Heitz, A. Schliwa, R.L. Sellin, F. Guffarth, D. Bimberg, Phys. Rev. B **68**, 035331 (2003)
- [38] T. Nakai, S. Iwasaki, K. Yamaguchi, Jpn. J. Appl. Phys. **43**, 2122 (2004)
- [39] A.J. Williamson, L.W. Wang, A. Zunger, Phys. Rev. B **62**, 12963 (2000)
- [40] R. Resta, Phys. Rev. B **16**, 2717 (1977)
- [41] L.-W. Wang, J. Kim, A. Zunger, Phys. Rev. B **59**, 5678 (1999)
- [42] T. Nakai, K. Yamaguchi, Jpn. J. Appl. Phys. **44**, 3803 (2005)
- [43] N.N. Ledentsov, J. Bohrer, M. Beer, F. Heinrichsdorff, M. Grundmann, D. Bimberg, S.V. Ivanov, B.Ya. Meltser, S.V. Shaposhnikov, I.N. Yassievich, N.N. Faleev, P.S. Kop'ev, Zh.I. Alferov, Phys. Rev. B **52**, 14058 (1995)
- [44] C.D. Simserides, U. Hohenester, G. Goldone, E. Molinari, Phys. Rev. B **62**, 13657 (2000)
- [45] T. Saiki, K. Matsuda, S. Nomura, M. Mihara, Y. Aoyagi, S. Nair, T. Takagahara, J. Electron Microsc. **53**, 193 (2004)
- [46] Q. Wu, R.D. Grober, D. Gammon, D.S. Katzer, Phys. Rev. B **62**, 13022 (2000)
- [47] D. Gammon, E.S. Snow, D.S. Katzer, Appl. Phys. Lett. **67**, 2391 (1995)
- [48] S.V. Nair, T. Takagahara, Phys. Rev. B **55**, 5153 (1997)
- [49] M.F. Crommie, C.P. Lutz, D.M. Eigler, Nature **363**, 524 (1993)
- [50] M.F. Crommie, C.P. Lutz, D.M. Eigler, Science **262**, 218 (1993)
- [51] M. Morgenstern, J. Klijn, C. Meyer, M. Getzlaff, R. Adelung, R.A. Romer, K. Rossnagel, L. Kipp, M. Skibowski, R. Wiesendanger, Phys. Rev. Lett. **89**, 136806 (2002)
- [52] C. Meyer, J. Klijn, M. Morgenstern, R. Wiesendanger, Phys. Rev. Lett. **91**, 076803 (2003)
- [53] K. Kanisawa, M.J. Butcher, Y. Tokura, H. Yamaguchi, Y. Hirayama, Phys. Rev. Lett. **87**, 196804 (2001)
- [54] C. Chicanne, T. David, R. Quidant, J.C. Weeber, Y. Lacroute, E. Bourillot, A. Dereux, G. Colas des Francs, C. Girard, Phys. Rev. Lett. **88**, 097402 (2002)
- [55] D. Heitmann, J.P. Kotthaus, Phys. Today **46**, 56 (1993)

- [56] A. Lorke, J.P. Kotthaus, K. Ploog, Phys. Rev. Lett. **64**, 2559 (1990)
- [57] W. Hansen, T.P. Smith III, K.Y. Lee, J.A. Brum, C.M. Knoedler, J.M. Hong, D.P. Kern, Phys. Rev. Lett. **62**, 2168 (1989)
- [58] S. Nomura, Y. Aoyagi, Phys. Rev. Lett. **93**, 096803 (2004)
- [59] V. Kukushkin, K. von Klitzing, K. Ploog, V.B. Timofeev, Phys. Rev. B **40**, 7788 (1989)
- [60] V. Kukushkin, R.J. Haug, K. von Klitzing, K. Ploog, Phys. Rev. Lett. **72**, 736 (1994)
- [61] S. Nomura, Y. Aoyagi, Surf. Sci. **529**, 171 (2003)
- [62] S. Nomura, T. Nakanishi, Y. Aoyagi, Phys. Rev. B **63**, 165330 (2001)
- [63] A. Kumar, S.E. Laux, F. Stern, Phys. Rev. B **42**, 5166 (1990)
- [64] M.P. Stopa, Phys. Rev. B **54**, 13767 (1996)
- [65] D. Gammon, E.S. Snow, B.V. Shanabrook, D.S. Katzer, D. Park, Science **273**, 87 (1996)
- [66] M. Grundmann, J. Christen, N.N. Ledentsov, J. Bohrer, D. Bimberg, S.S. Ruvimov, P. Werner, U. Richter, U. Gosele, J. Heydenreich, V.M. Ustinov, A.Yu. Egorov, A.E. Zhukov, P.S. Kop'ev, Zh.I. Alferov, Phys. Rev. Lett. **74**, 4043 (1995)
- [67] A. Buyanova, W.M. Chen, G. Pozina, J.P. Bergman, B. Monemar, H.P. Xin, C.W. Tu, Appl. Phys. Lett. **75**, 501 (1999)
- [68] M. Kondow, K. Uomi, A. Niwa, T. Kitatani, S. Watahiki, Y. Yazawa, Jpn. J. Appl. Phys. **35**, 1273 (1996)
- [69] D. Gollub, M. Fischer, M. Kamp, A. Forchel, Appl. Phys. Lett. **81**, 4330 (2002)
- [70] M. Kawaguchi, T. Miyamoto, E. Gouardes, D. Schlenker, T. Kondo, F. Koyama, K. Iga, Jpn. J. Appl. Phys. **40**, L744 (2001)
- [71] F. Masia, A. Polimeni, G.B.H. von Hogerthal, M. Bissiri, M. Capizzi, P.J. Klar, W. Stolz, Appl. Phys. Lett. **82**, 4474 (2003)
- [72] S. Francoeur, S.A. Nikishin, C. Jin, Y. Qiu, H. Temkin, Appl. Phys. Lett. **75**, 1538 (1999)
- [73] A. Moto, S. Tanaka, N. Ikoma, T. Tanabe, S. Takagishi, M. Takahashi, T. Katsuyama, Jpn. J. Appl. Phys. **38**, 1015 (1999)
- [74] J. Sik, M. Schubert, G. Leibiger, V. Gottschalch, G. Wagner, J. Appl. Phys. **89**, 294 (2001)
- [75] K. Matsuda, T. Saiki, S. Takahashi, A. Moto, M. Takagishi, Appl. Phys. Lett. **78**, 1508 (2001)
- [76] M. Takahashi, A. Moto, S. Tanaka, T. Tanabe, S. Takagishi, K. Karatani, M. Nakayama, K. Matsuda, T. Saiki, J. Cryst. Growth **221**, 461 (2001)
- [77] M. Mintairov, T.H. Kosel, J.L. Merz, P.A. Blagnov, A.S. Vlasov, V.M. Ustinov, R.E. Cook, Phys. Rev. Lett. **87**, 277401 (2001)
- [78] L. Grenouillet, C. Bru-Chevallier, G. Guillot, P. Gilet, P. Duvaut, C. Vannuffel, A. Milion, A. Chenevas-Paule, Appl. Phys. Lett. **76**, 2241 (2000)
- [79] X.D. Luo, J.S. Huang, Z.Y. Xu, C.L. Yang, J. Liu, W.K. Ge, Y. Zhang, A. Mascarenhas, H.P. Xin, C.W. Tu, Appl. Phys. Lett. **82**, 1697 (2003)
- [80] Y.J. Wang, X. Wei, Y. Zhang, A. Mascarenhas, H.P. Xin, Y.G. Hong, C.W. Tu, Appl. Phys. Lett. **82**, 4453 (2003)

Progress in Nano-Electro-Optics VI  
Nano-Optical Probing, Manipulation, Analysis, and Their  
Theoretical Bases

Ohtsu, M. (Ed.)

2008, XIV, 174 p. 107 illus., Hardcover

ISBN: 978-3-540-77894-3